

**Investigating Accuracy of the Reconfigurable Optical Computer (ROC) in
Metatronics for Solving Partial Differential Equations**

by Joseph Warren Crandall

B.S. in Computer Science & Physics, May 2017, The George Washington University

A Thesis submitted to

The Faculty of
The School of Engineering & Applied Science
of the George Washington University
in partial fulfillment of the requirements
for the degree of Master of Science

May 19, 2019

Thesis directed by

Volker J. Sorger
Associate Professor of Electrical & Computer Engineering

ProQuest Number: 13864207

All rights reserved

INFORMATION TO ALL USERS

The quality of this reproduction is dependent upon the quality of the copy submitted.

In the unlikely event that the author did not send a complete manuscript and there are missing pages, these will be noted. Also, if material had to be removed, a note will indicate the deletion.



ProQuest 13864207

Published by ProQuest LLC (2019). Copyright of the Dissertation is held by the Author.

All rights reserved.

This work is protected against unauthorized copying under Title 17, United States Code
Microform Edition © ProQuest LLC.

ProQuest LLC.
789 East Eisenhower Parkway
P.O. Box 1346
Ann Arbor, MI 48106 – 1346

© Copyright 2019 Joseph Warren Crandall
All rights reserved

Dedication

This work is dedicated to my family and friends who motivate and support me. Thank you all.

Acknowledgments

The research environment at GW has provided me with time, equipment, and colleagues to learn from and collaborate with, some of which I would like to thank explicitly. Engin Kayraklioglu has been instrumental in the development of the first iteration of the ROC software stack which includes SPICE models, usage of the Lumerical API, and is now starting to focus on error correction and will eventually involve ROC drivers. I hope to keep collaborating with you on this GitHub repository. Shuai Sun has been my desk mate ever since I started working in the OPEN Lab. He has led the fabrication of photonic ROC as well as being one of the first people in the Lab to learn the Lumerical simulation tool set. I have asked Shuai many questions and he has answered even more. Even since the arrival of our Postdoc Mario Miscuglio, my research has been accelerated. Mario's depth and breath of photonic and metatronic knowledge and modeling skill has motivated me to improve me own. PI Tarek El-Ghazawi has provided extensive edits throughout the thesis process and I greatly appreciate his input. Finally I would like to thank my PI Volker Sorger for both his edits during the thesis writing process and for pushing this team aggressively and helping to put us on the map. Thank you all.

Abstract of Thesis

Investigating Accuracy of the Reconfigurable Optical Computer (ROC) in Metatronics for Solving Partial Differential Equations

Nanoscale area metatronic analog circuitry utilizes relative permittivity between material interfaces to confine and direct electric displacement field and electric displacement current density operating at $f = 193$ THz. This is interesting because we have shown that we can map an analog finite difference algorithm into metatronics, while avoiding the partial differential equation (PDE) decreasing accuracy at increasing node density issue encountered by microscale area photonic analog circuitry also operating at $f = 193$ THz

The microscale area electronic analog circuitry, operating at $f \approx 300$ GHz, and the nanoscale area metatronic circuitry both exhibit partial differential equation (PDE) solution increasing accuracy at increasing node density, in the same fashion to a software driven digital hardware based finite difference algorithm PDE solution approaching the accuracy of analytically derived pde solution through increased node density.

With the proper allocation of hardware source and sample location for the metatronic and electronic circuitry we have shown that both analog hardwares can operate in constant time $O(1)$, and thus merit integration into larger software based parallel multi grid methods. However, the larger metatronic operating frequency increases its Shannon–Hartley theorem limited repetition rate (clock speed) into the Terahertz, while the smaller electronic operating frequency relegates its Shannon–Hartley theorem limited repetition rate (clock speed) to the Gigahertz.

Through the use of resistors, capacitors, and inductors the electronic circuit can be reconfigured to solve Laplace, Poisson, diffusion, and wave partial differential equations. In principal the metatronic circuit can bias its epsilon near zero material to induce changes in its relative permittivity inducing metatronic capacitance and inductance. Although this has not been shown in simulation at this point. Metatronic resistance occurs when the imaginary components of the epsilon near zeros material is not equal to zero.

It is difficult to understand all of the constraints one must account for in hardware design if one does not fully understand the final application the hardware solves. Any PDE solution method that employs a mesh or grid, and ultimately a finite difference, in the process of generating a solution suffers from discretization error. The only method that does not are analytically derived solutions, which is why it is important to understand what makes analytical methods challenging and not widely used, because in theory, the PDE solutions they produce will be the most accurate.

The mapping of a digital finite difference algorithm to an analog circuit requires the operational frequency and corresponding wavelengths size to exceed the diameter of the analog grid. This relationship determines the behavior of the electronic lumped, photonic distributed, and metatronic lumped grid based algorithms accuracy when solving PDEs. A lumped circuit node directs current, or displacement current density based on the direction and magnitude that the node's neighborhood is directing their current or displacement current density. In the case of a lumped circuit the neighborhood of nodes is the entire circuit. In a distributed circuit each nodes neighborhood is defined as all the nodes within one wavelength of operation. If the distance between two adjacent nodes is greater than one wavelength of operation, as is the case in the current fabricated photonic circuit, then all of the nodes are isolated. An isolated node does not feel the effects of a neighborhood because it has none, and instead must determine a new way to direct its optical intensity. The current practice is to engineer the geometry of the node to direct an equal amount of incoming optical intensity into all of the outgoing waveguides. This equal splitting is fixed in passive silicon.

The effects on PDE accuracy of lumped neighborhood based variable splitting versus distributed isolated node fixed splitting begin to reveal themselves as the number of nodes in the circuit increases. Changes in grid size, density, or both point to a trend of increasing accuracy for the lumped element circuits and decreasing accuracy for the isolated node circuits when compared to analytical continuous and digital numerical discrete pde solutions.

This Thesis' findings encompassing the combined advantages of increasing accuracy, preserved reconfigurability, increased repetition rate, and decreased footprint for meta-tronic circuits solving partial differential equations paves the wave for experimental fabricated demonstrations to validate this theoretical work.

Table of Contents

Dedication	iii
Acknowledgments	iv
Abstract of Thesis	v
List of Figures	xi
List of Abbreviations	xv
Glossary of Terms	xvii
Chapter 1: Introduction	1
1.1 What is ROC	1
1.2 Papers, Patents, and Challenges	2
1.3 Deliverables	3
1.3.1 Year 1 from October 2017 to September 2018	4
1.3.2 Year 2 from October 2018 to September 2019	4
1.4 Partial Differential Equation Solution Methods	4
1.5 ROC Fundamentals	8
1.5.1 ROC	8
1.5.2 Photonic	9
1.5.3 Metatronic	10
1.6 Accuracy	12

Chapter 2: Mathematics & Physics Underlying the Computational Model	15
2.1 Computational Time Complexity Requirements	15
2.2 Analytical Derivation PDE Solution	15
2.2.1 Analytical Solution	15
2.2.2 Physical Units	17
2.3 Discrete Numerical PDE Solution	18
2.3.1 Numerical Solution	18
2.3.2 Discretization Error	19
2.4 Electrical Analog PDE Solution	20
2.4.1 Electrical Elements	20
2.4.2 Difference Equation Approximation	21
2.5 Photonic Analog PDE Solution	23
2.5.1 Limitations of Passive Photonic Difference Equation Approximation	23
2.6 Metatronic Analog PDE Solution	27
2.6.1 Device Physics	27
2.6.2 Finite Difference Equation Equivalence	28
2.6.3 Solution of Laplace Equation	29
2.6.4 Monolythic Integration	31
2.6.5 ITO based Performance	34
2.6.6 Near Field Displacement Measurement	35
2.7 Supplemental Material	36
2.7.1 Analytical Solution to a Laplacian Steady State Heat Transfer PDE .	36

2.7.2	Mapping of Difference Equation Approximation to Electrical Resistance Mesh	41
Chapter 3: Future Work		44
3.1	Future Work	44
3.1.1	Year 3 from October 2019 to September 2020	44
3.1.2	Year 4 from October 2020 to September 2021	44
3.2	Concluding Thoughts	44
References		50
Appendix A: Software Development		52
A.1	GitHub	52
Appendix B: Computational Models		53
B.1	Computation	53
B.1.1	Computing Resources	53
B.2	Simulation Tools and Applications	53
B.2.1	COMPSOL Multiphysics	53
B.2.2	Lumerical Interconnect	53
B.2.3	Wolfram Mathematica	53
B.2.4	Simulation Program with Integrated Circuit Emphasis (SPICE)	54

List of Figures

1.1	The top row of this figure illustrates the traditional options available for solving a PDE through (A) analytical, (B) numerical, and (C) analog electrical PDE solving paradigms, while the bottom row illustrates the recon-figurations of an analog electrical discrete solution for different classes of partial differential equation (PDE)s including (D) Laplace, (E) Poisson, (F) diffusion, and (G) wave equation.	7
1.2	The Laplace PDE dependent physical units and equations for grid com-ponents in the electronic mesh, photonic ROC, and metatronic ROC are shown. The electrical and metatronic circuits operate as lumped elements and the photonic circuit operates as a distributed circuit. The equation units of metatronic ROC electric displacement current density are as follows: $\tilde{\epsilon}$ material permittivity [Fm^{-1}], $\omega = 2\pi f$ Angular Frequency [Hz], $E(\omega)$ electrical field [Vm^{-1}] or [NC^{-1}]. It is also important to distinguish be-tween which photonic quantity's are measurable. We measure optical in-tensity through the use of a Y branch and a grating along each edge at the output of each optical node.	9
1.3	The top row of this figure illustrates the different analog grid based PDE solving technologies including (A) the original electrical analog, (B) the silicon photonics implementation, and (C) the Metatronic Implementation. The columns represent the different configurations of the grid, that give the “reconfigurable” optical computer its name, allowing for Poisson, dif-fusion, and wave configurations. As you probably have noticed, there is no photonic schematic showing an equivalence to (D) electrical capacitance, or (G) electrical inductance, but there is (F) metatronic capacitance and (H) metatronic inductance. Table (E) shows the physical effects utilized in the technologies and is shown in larger form in Figure 1.2. In the language of graph theory, a node is a grid point within the mesh, and an edge is a connection between grid points.	11
1.4	Electronic analog exhibits lumped element, neighborhood defined splitting, and increased accuracy from increased node density.	12
1.5	The metatronic circuit exhibits lumped element, neighborhood defined split-ting, and therefore increasing accuracy from increased node density all at a smaller operational wavelength than the electrical analog.	13

- 2.1 Computation time complexity of a single PDE analog grid solution iteration in the three analog physics technologies could be incorporated into a **(D)** parallelized multi grid method using finite difference method operating at logarithmic time, polylogarithmic time, or fractional power time depending on the course fine grid traversal utilized. For one of the analog system to remain in the constant time domain certain hardware requirements must be met. If we assume that n is the number of nodes in a one dimension side of an grid and h is the length of an edge between nodes in the grid, we can see that the number of **(A)** current, **(B)** optical intensity, and **(C)** displacement current density hardware source locations are needed to set boundary conditions, shown on the top row, and we can see the needed number of **(H)** current, **(I)** optical intensity, and **(J)** displacement current density sample locations are required to read out a PDE analog solution. With all of these sources and samples operating in parallel. The grid length scales for the **(E)** electrical **(G)** metatronic execution step remain within one operation wavelength for both technologies, and thus remain in constant time, where as the **(F)** photonic grid length scale exceeds its operational wavelength, and thus requires k iterations to traverse the diameter of the grid 16
- 2.2 **(A)** The four boundaries of $\psi(x, y)$ are defined in terms of the x and y axis. **(B)** The one non-zero boundary condition and three zero boundary conditions for the $\varphi_3(x, y)$ solution component of $\varphi(x, y)$. **(C)** Plot of $\psi_{3,n}(x, y)$ with $n = 1$, $L = 5$ and $H = 5$ with the continuous solution shown in the z axis. 17
- 2.3 The finalized COMSOL geometry has one domain, 4 boundaries, and 4 vertices. **(A)** The physics controlled normal element size mesh consists of 68 domain elements and 20 boundary elements, **(B)** 578 domain elements and 60 boundary elements, and **(C)** 6282 domain elements and 200 boundary elements. The number of degrees of freedom solved for is **(D)** 157 plus 44 internal DOFs and the solution is solved for in 1 seconds, **(E)** DOFs 1217 plus 124 internal DOFs solved for in 2 seconds, and **(F)** DOFs 12765 plus 404 internal DOFs solved for in 1 second. 18
- 2.4 **(A)** Plot of $\psi_{3,n}(x, y)$ with $L = 5$ and $H = 5$ with the the discretized mesh $2^1 = 2$ blue, $2^2 = 4$ green, $2^3 = 8$ yellow, $2^4 = 16$ orange, and $2^5 = 32$ purple solutions shown in the z axis. **(B)** The right side view is shown. . . . 20

- 2.5 **(A)** The derivative of the function φ at point P_0 is expressed through the differences of φ between points P_0 and $P_1, P_2, P_3,$ and P_4 . The distance between P_0 and P_1 is labeled h_1 . The scalar function ϵ for vector function φ between points P_0 and $P_1, P_2, P_3,$ and P_4 is labeled ϵ_1 between P_0 and P_1 . **(B)** The voltage $V[V]$ at point P_0 is expressed as V_0 . The current $I[A]$ and Resistance $R[\Omega]$ between points P_0 and P_1 is expressed as I_1 and R_1 respectively. The same naming conventions apply for $P_2, P_3,$ and P_4 . I_0 is the input current and R_0 is defined in terms of other resistances, and therefor not shown on the diagram. **(C)** Poisson class electrical 16 node resistance network with the ability to apply a current at each node. 21
- 2.6 Benchmarking the accuracy of a spice circuit simulator analog mesh 2D PDE solution against an analytically solved 2D PDE solution of a Laplace heat transfer problem. Mesh based solutions are scaled linearly from 2 up to the problem size N with problem sizes 8, 16, 32, and 64 plotted. Average difference is calculated by comparing the spice based voltage value at a mesh point coordinate to the value sampled from the continuous analytical solution at the same coordinate. Then the difference from all Simulation Program with Integrated Circuit Emphasis (SPICE) analytical coordinate comparisons in a mesh are averaged, resulting in a single average difference point which is plotted for each mesh for each problem size. This average difference is the measure of accuracy with a higher difference resulting from a greater deviation in the spice solution from the "true north" analytical solution. Thus a lower average difference implies a higher accuracy with a value of 0 being a perfect match. *Analytical solutions not scaled for volts yet. *Program crashed at Mesh 49 on problem 64. 24
- 2.7 The **(A)** geometrically engineered fixed optical loss fabricated into waveguide geometries allows for **(B)** Lumerical INTERCONNECT passive photonic ROC simulations to approximately solve Laplace class PDEs. However, unlike the electrical mesh, each photonic ROC splitting node, composed of 4 ring resonators and a central splitter, due to its micrometer size and distributed element model behavior is effectively isolated from its neighborhood of surrounding nodes due to the limit of what a single wavelength of light can reach in a discrete time step. The **(C)** metatronic splitting is neighborhood defined and can be **(D)** simulated with COMSOL to showcase the ENZ confinement of displacement current density. 26
- 2.8 The figure shows a **(A)** finite difference node, a **(B)** metatronic resistive node with displacement current density sampling locations, and a **(C)** metatronic material relative permittivity reconfigurability key. 28

2.9	The epsilon-near-zero (ENZ) boxes in this simulation are $100 \text{ nm} \times 100 \text{ nm}$ and the epsilon very large (EVL) groves are 10 nm wide where (A) contains 4 by 4 ENZ boxes and (B) contains 8 by 8. One can see that at longer length scales the electric displacement field continues to produce the form of the PDE solution, but the containment of displacement current density within the EVL air groves is weakened.	31
2.10	The (A) ENZ wavelength, (B) Electrostatic doping, and (C) Scattering Time (τ_{sc}) as function of process parameters (Oxygen flow-rate and deposition time). The (D) Drude model of ITO film, sputtered with an initial electron doping of 10^{19} cm^{-3} and $\Gamma = \frac{1}{\tau_{sc}}$, for an increasing carrier modulation (blue to red).	32
2.11	The metatronic solution accuracy as function of mesh density and size when compared to an discrete PDE solution.	34
2.12	Schematic representation of a "Nanophotonic Probe". An impinging radiation excites a fluorescent molecule, creating a local near field, which produces an electric displacement in the metatronic circuit. The displacement is probed by the tips of a probe card, in a campanile tip aperture nSOM configuration.	35

List of Abbreviations

AIM Photonics	American Institute for Manufacturing Integrated Photonics	23
ASIC	application-specific integrated circuit	2
ENZ	epsilon-near-zero	xiii, xiv, 12, 26–28, 30, 31
EVL	epsilon very large	xiv, 27, 31
HPCL	High-Performance Computing Lab	2
IEEE	Institute of Electrical and Electronics Engineers	1
IRDS	International Roadmap For Devices And Systems	1
ITO	Indium tin oxide	12, 28, 30
ITRS	International Technology Roadmap for Semiconductors	1
MIMO	multiple-input and multiple-output	7
NIC	Nanofabrication and Imaging Center	23
NSF	National Science Foundation	2
ODE	ordinary differential equation	5
OPEN	Orthogonal Physics Enabled Nanophotonics	2, 23
PDE	partial differential equation v–vii, xi, xiii, xiv, 2, 5–9, 11, 15, 24–26, 30, 31, 34, 43,	
	53	
RAISE	Research Advanced by Interdisciplinary Science and Engineering	2

ROC Reconfigurable Optical Computer xi, xiii, 1, 2, 8, 9, 11, 19, 23, 26, 53

SPICE Simulation Program with Integrated Circuit Emphasis x, xiii, 24, 54

VLSI Very Large Scale Integration 2, 7

functions such as the Bessel functions and the gamma function are usually allowed, and often so are infinite series and continued fractions. On the other hand, limits in general, and integrals in particular, are typically excluded. If an analytic expression involves only the algebraic operations (addition, subtraction, multiplication, division, and exponentiation to a rational exponent) and rational constants then it is more specifically referred to as an algebraic expression. 5

application-specific integrated circuit An application-specific integrated circuit is an integrated circuit (IC) customized for a particular use, rather than intended for general-purpose use. 2

Big O notation Big O notation is a mathematical notation that describes the limiting behavior of a function when the argument tends towards a particular value or infinity. It is a member of a family of notations invented by Paul Bachmann, Edmund Landau, and others, collectively called Bachmann–Landau notation or asymptotic notation. In computer science, big O notation is used to classify algorithms according to how their running time or space requirements grow as the input size grows. In analytic number theory, big O notation is often used to express a bound on the difference between an arithmetical function and a better understood approximation; a famous example of such a difference is the remainder term in the prime number theorem. Big O notation characterizes functions according to their growth rates: different functions with the same growth rate may be represented using the same O notation. The letter O is used because the growth rate of a function is also referred to as the order of the function. A description of a function in terms of big O notation usually only provides an upper bound on the growth rate of the function. Associated with big O notation are several related notations, using the symbols o , Ω , ω , and Θ , to describe other kinds of bounds on asymptotic growth rates. 5

co-processor A coprocessor is a computer processor used to supplement the functions of the primary processor (the CPU). Operations performed by the coprocessor may be floating point arithmetic, graphics, signal processing, string processing, cryptography or I/O interfacing with peripheral devices. By offloading processor-intensive tasks from the main processor, coprocessors can accelerate system performance. 8

COMPSOL Multiphysics COMSOL Multiphysics is a cross-platform finite element analysis, solver and multiphysics simulation software. It allows conventional physics-based user interfaces and coupled systems of partial differential equations (PDEs). COMSOL provides an IDE and unified workflow for electrical, mechanical, fluid, and chemical applications. An API for Java and LiveLink for MATLAB may be used to control the software externally, and the same API is also used via the Method Editor. x, 11, 53

Conjugate gradient method In mathematics, the conjugate gradient method is an algorithm for the numerical solution of particular systems of linear equations, namely those whose matrix is symmetric and positive-definite. The conjugate gradient method is often implemented as an iterative algorithm, applicable to sparse systems that are too large to be handled by a direct implementation or other direct methods such as the Cholesky decomposition. Large sparse systems often arise when numerically solving partial differential equations or optimization problems. The conjugate gradient method can also be used to solve unconstrained optimization problems such as energy minimization. It was mainly developed by Magnus Hestenes and Eduard Stiefel who programmed it on the Z4. The biconjugate gradient method provides a generalization to non-symmetric matrices. Various nonlinear conjugate gradient methods seek minima of nonlinear equations. 5

Dennard scaling Dennard scaling, also known as MOSFET scaling, is a scaling law based on a 1974 paper co-authored by Robert H. Dennard, after whom it is named. Origin-

nally formulated for MOSFETs, it states, roughly, that as transistors get smaller, their power density stays constant, so that the power use stays in proportion with area; both voltage and current scale (downward) with length..... 1

displacement current density In electromagnetism, displacement current density is the quantity $\frac{\partial D}{\partial t}$ appearing in Maxwell's equations that is defined in terms of the rate of change of D , the electric displacement field. Displacement current density has the same units as electric current density, and it is a source of the magnetic field just as actual current is. However it is not an electric current of moving charges, but a time-varying electric field. In physical materials (as opposed to vacuum), there is also a contribution from the slight motion of charges bound in atoms, called dielectric polarization..... 4

distributed element model In electrical engineering, the distributed element model or transmission line model of electrical circuits assumes that the attributes of the circuit (resistance, capacitance, and inductance) are distributed continuously throughout the material of the circuit. This is in contrast to the more common lumped element model, which assumes that these values are lumped into electrical components that are joined by perfectly conducting wires. In the distributed element model, each circuit element is infinitesimally small, and the wires connecting elements are not assumed to be perfect conductors; that is, they have impedance. Unlike the lumped element model, it assumes non-uniform current along each branch and non-uniform voltage along each node. The distributed model is used at high frequencies where the wavelength becomes comparable to the physical dimensions of the circuit, making the lumped model inaccurate 10, 23

Drude model The Drude model of electrical conduction was proposed in 1900 by Paul Drude to explain the transport properties of electrons in materials (especially metals). The model, which is an application of kinetic theory, assumes that the microscopic

behavior of electrons in a solid may be treated classically and looks much like a pin-ball machine, with a sea of constantly jittering electrons bouncing and re-bouncing off heavier, relatively immobile positive ions..... 28

finite difference method In mathematics, finite-difference methods (FDM) are numerical methods for solving differential equations by approximating them with difference equations, in which finite differences approximate the derivatives. FDMs are thus discretization methods. FDMs convert a linear (non-linear) ODE/PDE into a system of linear (non-linear) equations, which can then be solved by matrix algebra techniques. The reduction of the differential equation to a system of algebraic equations makes the problem of finding the solution to a given ODE ideally suited to modern computers, hence the widespread use of FDMs in modern numerical analysis[1]. Today, FDMs are the dominant approach to numerical solutions of partial differential equations..... 5, 8

Indium tin oxide Indium tin oxide (ITO) is a ternary composition of indium, tin and oxygen in varying proportions. Depending on the oxygen content, it can either be described as a ceramic or alloy. Indium tin oxide is typically encountered as an oxygen-saturated composition with a formulation of 74% In, 18% O₂, and 8% Sn by weight. Oxygen-saturated compositions are so typical, that unsaturated compositions are termed oxygen-deficient ITO. It is transparent and colorless in thin layers, while in bulk form it is yellowish to grey. In the infrared region of the spectrum it acts as a metal-like mirror. Indium tin oxide is one of the most widely used transparent conducting oxides because of its two main properties: its electrical conductivity and optical transparency, as well as the ease with which it can be deposited as a thin film. As with all transparent conducting films, a compromise must be made between conductivity and transparency, since increasing the thickness and increasing the concentration of charge carriers increases the material's conductivity, but decreases its

transparency. Thin films of indium tin oxide are most commonly deposited on surfaces by physical vapor deposition. Often used is electron beam evaporation, or a range of sputter deposition techniques. 12

Institute of Electrical and Electronics Engineers The Institute of Electrical and Electronics Engineers (IEEE) is a professional association with its corporate office in New York City[3] and its operations center in Piscataway, New Jersey. It was formed in 1963 from the amalgamation of the American Institute of Electrical Engineers and the Institute of Radio Engineers. Today, the organization’s scope of interest has expanded into so many related fields, that it is simply referred to by the letters I-E-E-E (pronounced Eye-triple-E), except on legal business documents. As of 2018, it is the world’s largest association of technical professionals with more than 423,000 members in over 160 countries around the world. Its objectives are the educational and technical advancement of electrical and electronic engineering, telecommunications, computer engineering, and allied disciplines. 1

International Roadmap For Devices And Systems This initiative focuses on an International Roadmap for Devices and Systems (IRDS) through the work of roadmap teams closely aligned with the advancement of the devices and systems industries. Led by an international roadmap committee (IRC), International Focus Teams (IFTs) will collaborate in the development of a roadmap, and engage with other segments of the IEEE, such as Rebooting Computing, and related industry communities, in complementary activities to help ensure alignment and consensus across a range of stakeholders, such as, Academia, Consortia, Industry, and National laboratories. IEEE, the world’s largest technical professional organization dedicated to advancing technology for humanity, through the IEEE Standards Association (IEEE-SA) Industry Connections (IC) program, supports the IRDS to ensure alignment and consensus across a range of stakeholders to identify trends and develop the roadmap for all of

the related technologies in the computer industry. 1

International Technology Roadmap for Semiconductors The International Technology Roadmap for Semiconductors (ITRS) is a set of documents produced by a group of semiconductor industry experts. These experts are representative of the sponsoring organisations which include the Semiconductor Industry Associations of the United States, Europe, Japan, South Korea and Taiwan. The documents produced carry this disclaimer: "The ITRS is devised and intended for technology assessment only and is without regard to any commercial considerations pertaining to individual products or equipment". The documents represent best opinion on the directions of research and time-lines up to about 15 years into the future for the following areas of technology: System drivers/design, Test test equipment, Front-end processes, Process integration, devices and structures, Radio frequency, analog/mixed-signal technologies, Microelectromechanical systems (MEMS), Photolithography, IC interconnects, Factory integration, Assembly packaging, Environment, safety health, Yield enhancement, Metrology, Modeling simulation, Emerging research devices, and Emerging research materials. As of 2017, ITRS is no longer being updated. 1

Koomey's law Koomey's law describes a long-term trend in the history of computing hardware. The number of computations per joule of energy dissipated has been doubling approximately every 1.57 years. This trend has been remarkably stable since the 1950s (R^2 of over 98%) and has been somewhat faster than Moore's law. Jonathan Koomey articulated the trend as follows: "at a fixed computing load, the amount of battery you need will fall by a factor of two every year and a half. 1

linear interpolation In mathematics, linear interpolation is a method of curve fitting using linear polynomials to construct new data points within the range of a discrete set of known data points. 41

lumped element The lumped element model (also called lumped parameter model, or lumped component model) simplifies the description of the behaviour of spatially distributed physical systems into a topology consisting of discrete entities that approximate the behaviour of the distributed system under certain assumptions. It is useful in electrical systems (including electronics), mechanical multibody systems, heat transfer, acoustics, etc. Mathematically speaking, the simplification reduces the state space of the system to a finite dimension, and the partial differential equations (PDEs) of the continuous (infinite-dimensional) time and space model of the physical system into ordinary differential equations (ODEs) with a finite number of parameters.

27

Metatronic Metamaterial-inspired optical nanocircuitry follows the success of modularization in electronics, individual nanoparticles are treated as lumped circuit elements (for example, nanocapacitors, nanoinductors, and nanoresistors) whose impedance is defined in terms of how the nanoparticle modifies the flux of the displacement current, as a function of the applied electric potential. In addition, in analogy with classical circuit wires, lumped elements in metatronic circuits are usually interconnected via D-dot wires, that is, optical wires designed to confine and “guide” the flow of the displacement current. This methodology enables the design of complex nanoparticle systems by using techniques and tools developed for the design of electronic circuits.[1]

8

Moore’s law Moore’s law is the observation that the number of transistors in a dense integrated circuit doubles about every two years. The observation is named after Gordon Moore, the co-founder of Fairchild Semiconductor and CEO of Intel, whose 1965 paper described a doubling every year in the number of components per integrated

circuit and projected this rate of growth would continue for at least another decade. In 1975, looking forward to the next decade, he revised the forecast to doubling every two years. The period is often quoted as 18 months because of a prediction by Intel executive David House (being a combination of the effect of more transistors and the transistors being faster) 1

Multigrid method In mathematics, the conjugate gradient method is an algorithm for the numerical solution of particular systems of linear equations, namely those whose matrix is symmetric and positive-definite. The conjugate gradient method is often implemented as an iterative algorithm, applicable to sparse systems that are too large to be handled by a direct implementation or other direct methods such as the Cholesky decomposition. Large sparse systems often arise when numerically solving partial differential equations or optimization problems. The conjugate gradient method can also be used to solve unconstrained optimization problems such as energy minimization. It was mainly developed by Magnus Hestenes and Eduard Stiefel who programmed it on the Z4. The biconjugate gradient method provides a generalization to non-symmetric matrices. Various nonlinear conjugate gradient methods seek minima of nonlinear equations. 5

multiple-input and multiple-output In radio, multiple-input and multiple-output, or MIMO, is a method for multiplying the capacity of a radio link using multiple transmission and receiving antennas to exploit multipath propagation. MIMO has become an essential element of wireless communication standards including IEEE 802.11n (Wi-Fi), IEEE 802.11ac (Wi-Fi), HSPA+ (3G), WiMAX (4G), and Long Term Evolution (LTE 4G). More recently, MIMO has been applied to power-line communication for 3-wire installations as part of ITU G.hn standard and HomePlug AV2 specification. 7

Numerical analysis Numerical analysis is the study of algorithms that use numerical ap-

proximation (as opposed to general symbolic manipulations) for the problems of mathematical analysis (as distinguished from discrete mathematics). Numerical analysis naturally finds application in all fields of engineering and the physical sciences, but in the 21st century also the life sciences, social sciences, medicine, business and even the arts have adopted elements of scientific computations. As an aspect of mathematics and computer science that generates, analyzes, and implements algorithms, the growth in power and the revolution in computing has raised the use of realistic mathematical models in science and engineering, and complex numerical analysis is required to provide solutions to these more involved models of the world. Numerical analysis continues the long tradition of practical mathematical calculations, where modern numerical analysis does not seek exact answers, because exact answers are often impossible to obtain in practice. Instead, much of numerical analysis is concerned with obtaining approximate solutions while maintaining reasonable bounds on errors..... 5

optical intensity The optical intensity I , e.g. of a laser beam, is the optical power per unit area, which is transmitted through an imagined surface perpendicular to the propagation direction. The units of the optical intensity (or light intensity) are W/m^2 or (more commonly) W/cm^2 . The intensity is the product of photon energy and photon flux. It is sometimes called optical energy flux..... 8

ordinary differential equation In mathematics, an ordinary differential equation (ODE) is a differential equation containing one or more functions of one independent variable and the derivatives of those functions. The term ordinary is used in contrast with the term partial differential equation which may be with respect to more than one independent variable..... 5

passive optical A passive optical networks (PON) distinguishing feature is that it implements a point-to-multipoint architecture, in which unpowered fiber optic splitters are

used to enable a single optical fiber to serve multiple end-points. 25

Photonic Photonics is the physical science of light (photon) generation, detection, and manipulation through emission, transmission, modulation, signal processing, switching, amplification, and sensing. Though covering all light’s technical applications over the whole spectrum, most photonic applications are in the range of visible and near-infrared light. The term photonics developed as an outgrowth of the first practical semiconductor light emitters invented in the early 1960s and optical fibers developed in the 1970s. 8

post-Moore The (CMOS) world is ending next decade, so says the international technology roadmap for semiconductors. In the long term (2017 THROUGH 2024) ,while power consumption is an urgent challenge, its leakage or static component will become a major industry crisis in the long term, threatening the survival of CMOS technology itself, just as bipolar technology was threatened and eventually disposed of decades ago. [ITRS 2009/2010]. Unlike the situation at the end of the bipolar era, no technology is waiting in the wings. The technological barriers that need to be overcome include new materials and new structures. Materials such as III-V or germanium thin channels on silicon, or even semiconductor nanowires, carbon nanotubes, graphene or others may be needed. Three-dimensional architecture, such as vertically stackable cell arrays in monolithic integration, with acceptable yield and performance. [2] 8

probe card A probe card is an interface between an electronic test system and a semiconductor wafer. Typically the probe card is mechanically docked to a prober and electrically connected to a tester. Its purpose is to provide an electrical path between the test system and the circuits on the wafer, thereby permitting the testing and validation of the circuits at the wafer level, usually before they are diced and packaged. It consists, normally, of a printed circuit board (PCB) and some form of contact ele-

ments, usually metallic, but possibly of other materials as well.

12

RC time constant The RC time constant, also called tau, the time constant (in seconds) of an RC circuit, is equal to the product of the circuit resistance (in ohms) and the circuit capacitance (in farads), i.e. $\tau = RC$ 8

technology node The technology node (also process node, process technology or simply node) refers to a specific semiconductor manufacturing process and its design rules. Different nodes often imply different circuit generations and architectures. Generally, the smaller the technology node means the smaller the feature size, producing smaller transistors which are both faster and more power-efficient. Historically, the process node name referred to a number of different features of a transistor including the gate length as well as M1 half-pitch. Most recently, due to various marketing and discrepancies among foundries, the number itself has lost the exact meaning it once held. Recent technology nodes such as 22 nm, 16 nm, 14 nm, and 10 nm refer purely to a specific generation of chips made in a particular technology. It does not correspond to any gate length or half pitch. Nevertheless, the name convention has stuck and it's what the leading foundries call their nodes. 1

Very Large Scale Integration Very-large-scale integration (VLSI) is the process of creating an integrated circuit (IC) by combining hundreds of thousands of transistors or devices into a single chip. VLSI began in the 1970s when complex semiconductor and communication technologies were being developed. The microprocessor is a VLSI device. Before the introduction of VLSI technology most ICs had a limited set of functions they could perform. An electronic circuit might consist of a CPU, ROM, RAM and other glue logic. VLSI lets IC designers add all of these into one chip. . 2

Chapter 1 - Introduction

1.1 What is ROC

Reconfigurable Optical Computer (ROC) is research project undertaken by a collaboration between the OPEN Lab Team under the leadership of PI Volker Sorger and the HPCL Team under the leadership of PI Tarek El Ghazawi both based at the George Washington University through the funding of an NSF RAISE Grant working to understanding the physics of, develop software for, and fabricate an analog co-processor implemented in Silicon Photonics, and Optical Metatronics, with the goal of calculating approximate solutions to 4 classes of partial differential equations comprised of Laplace, Poisson, Diffusion, and Wave. The approximate accuracy of these solutions, the time required to attain them, the energy utilized in the computation, and the physical dimension of the fabricated chip are compared against analytically derived, and numerically computed solutions, as well against a previously researched electronic analog co-processor.

This research is part of a larger trend punctuated by the termination of the International Technology Roadmap for Semiconductors (ITRS) 2.0 report with its final 2015 publication [3]. The report published for decades comprised an amalgamation of the opinions of worlds leading semiconductor researchers and industry professionals and is arguably most known for setting expectations for semiconductor technology node scaling. However due to the challenges posed by the limits of Moore's law, the end of Dennard scaling, the slowing of Koomey's law, and the limits of Amdahl's Law.

The Institute of Electrical and Electronics Engineers (IEEE) has pivoted and released the International Roadmap For Devices And Systems (IRDS) 2017 edition [4]. In the report IRDS acknowledges that 2D scaling will reach fundamental limits beyond 2020 and as a solution they introduce three distinct eras of scaling, Geometrical (1975-2002), Equivalent (2003 ~ 2024), and 3D Power (2025 ~ 2040) with Equivalent Scaling (2003 ~ 2024) being defined by the "reduction of only horizontal dimension in conjunction with introduction of

new materials and new physical effects”. With ”new vertical structures replacing planar transistors”. Our research embraces this paradigm shift and falls within the scope of new materials and new physical effects. As of 2018 companies such as Xilinx have started to design processors with CPU, GPU, and FPGA architectures integrated [5], with the new question being which architecture is best for which task. The PDE co-processing capabilities of ROC fall within this trend.

1.2 Papers, Patents, and Challenges

The concept of an analog electronic mesh based computer applied to approximately solve partial differential equations was initially researched by G. Liebmann and colleagues in the 1950’s [6, 7]. In 2000, a programmable Very Large Scale Integration (VLSI) chip for analog solutions to PDEs was patented [8] that can be implemented using discrete components or as an application-specific integrated circuit (ASIC), hosted by a digital computer. In 2015 members of the High-Performance Computing Lab (HPCL) and Orthogonal Physics Enabled Nanophotonics (OPEN) lab and the filed a patent for an optical implementation of a PDE solving circuit implementation of Reconfigurable Optical Computer (ROC) [9].

Due to the focused time I have spent working on the 4 year (2017-2021) National Science Foundation (NSF) Research Advanced by Interdisciplinary Science and Engineering (RAISE) funded ROC project I have been able to uncover the underlying challenges I have been working to address as well as the ones that I have avoided in my goal of understanding accuracy. The ROC project is a product of larger research trend, partially encompassed by what I believe are two grand challenges.

The first being that CMOS technology surpassed analog alternatives in the 1970s because of its versatility and successful scaling, but decreasing CMOS 2D length scaling is ending during the 2020s, which is creating room for many alternative technologies to be proposed. This research space and funding created by the first challenge has allowed teams

to think fundamentally about how different algorithms perform computation. After working on the ROC project, I have come to the conclusion that I am sure many other researchers before me have concerning competitiveness encompassed in the second grand challenge.

Algorithms built into hardware must improve their computational time complexity compared to pure software-based implementations to make up for a loss of versatility, but how much versatility must the hardware provide for the effort to be worthwhile? I realize that algorithms built into hardware can have similar computational time complexity but improved energy consumption compared to pure software, but since I am focusing on accuracy as a metric of performance, I have not rigorously explore improvements in energy consumption as a metric of performance.

1.3 Deliverables

My thesis is composed of three chapters, Context Motivation, Mathematics Physics Underlying the Computation Model, and Future Work. The Context Motivation chapter discusses the intellectual discoveries the word builds on as well as challenges I am working to understand and address. The deliverable discussed correspond to my contributions to the yearly NSF specified project requirements and the structure of the written thesis. The partial differential equation solution methods cover the different ways one can go about solving a PDE and their limitations. The reconfigurable optical computer operation gives an overview of the physical photonic and metatronic analog coprocessors used to solve the PDEs, and accuracy covers the metric I use to evaluate the performance of the computer.

The second chapter, the Mathematics Physics Underlying the Computational Model contains the meat of my investigation. In a top down approach, I first ask the question where do the computational complexity gains originate from in an analog approach compared to a numerical discrete one? I then analytically derive a solution to a partial differential equation in order to understand where the difficulty in analytical approaches arises from and why an algorithmic analytical approach to pde solutions is challenging. Then I show the standard

numerical approach to a pde solution, followed by the original electrical analog approach and then the novel Photonic analog and Metatronic analog approaches. In the future work chapter I touch on what is expected by the NSF for the team to accomplish in the remaining two years as well as further Metatronic work that I am hoping to complete.

1.3.1 Year 1 from October 2017 to September 2018

During the first year of the NSF Project I created a branch of the "roc'grid'simulation" GitHub repository, initially developed by Engin Kayraklioglu, named boundaryConditions utilizing Python to generate spice based simulations of the electrical grid used by Lieberman to calculate their accuracy compared to an analytical solution to a Laplace PDE solution that I had derived. In order to better understand Liebmann's finite difference mapping technique I re derived his work which helped me understand the importance of a node and its neighborhood in terms of this relationships effect on accuracy and how it is altered with the physics of Photonics and Metatronics.

1.3.2 Year 2 from October 2018 to September 2019

During the second year I created COMSOL Models of the Metatronic ROC in order to study the effects of network size and density on their role in accuracy, leading to an understanding of the importance of displacement current density confinement. In my desire to showcase the possible computational advantages of ROC, I estimated computational time complexities values for the future processor in comparison to an electrical analog and how it could be utilized within a and discrete parallelized implementation.

1.4 Partial Differential Equation Solution Methods

Many computational problems in science and engineering are modeled via solving partial differential equations (PDEs) and are used to model physical phenomena such as fluid dynamics [10], electricity [11], magnetism [12], mechanics [13], optics [14], and heat flow

[15]. Some of these problems can not be solved for an Analytic expression and must rely on Numerical analysis to generate a final answer. Numerically derived solutions are commonly solved by first discretizing them into finite difference equations or finite elements through the use of the finite difference method. Iterative methods such as Conjugate gradient method or the adaptive Multigrid method are also often adopted in order to solve these equations [16]. Due to the large number of iterations in the recursive process required to attain more accurate solutions.

Due to the computational energy and time expense required to solve these equations techniques have been invented to simplify their calculation, such as transforming the PDEs into ordinary differential equations ordinary differential equation (ODEs) and much attention has been paid to creating efficient implementations of PDE solvers aimed at reducing the number of iterations [17, 18]. A PDE solution of heat flow over a homogeneous surface computed numerically requires the decomposition of the surface into an array of subsurfaces through the finite difference method, known as a computational mesh. Subsurfaces with smaller areas yield higher-precision results, but require more computations to arrive at a solution. As PDEs form the basis for many applications in scientific computing, efficiencies gained in this domain would be of great benefit to the scientific community [19].

The analog alternative to this digitally implemented numerical method traditionally utilized analogue circuits comprised of Resistor(R), Inductor(L), and Capacitor (C) elements that bypass the iterative recursive process by generating a mesh based solution in a single execution, equivalent to a computational complexity Big O notation of 1 or n (linear) depending on the speed of execution, once boundary conditions for the problem are set within the mesh, with the accuracy of the solution being determined by combination of the density of the mesh utilized and the area of the problem being solved for. This electrical analog finite difference architecture utilizes summation of current for computation and was originally developed to provide efficient computation of heat transfer [6] and oscillatory flow problems in aeronautical engineering [20], and has been shown to reduce the time

to solution through its elimination of the iterative processing steps which retard numerical methods.

Solving PDEs using Electrical Analogues requires an array of circuit elements suitably connected in order to yield electrical analogue of a PDE. A two-dimensional resistor array can generate an analog solution to a Laplace equation,

$$\nabla^2\varphi = 0 \tag{1.1}$$

while sampling current at nodes, we expand the class of PDEs to non zero solution Poisson Equations,

$$\nabla^2\varphi = ki \tag{1.2}$$

with the addition of capacitors at at nodes, we account for time dependence and expand the class of PDEs to Diffusion Equations,

$$\nabla^2\varphi = k\frac{\partial\varphi}{\partial t} \tag{1.3}$$

and by substituting capacitors for resistors and keeping capacitors at nodes, we expand the class of PDEs to Wave Equations,

$$\nabla^2\varphi = k\frac{\partial^2\varphi}{\partial t^2} \tag{1.4}$$

These classes of PDEs that can be accelerated by an electronic analog mesh based co-processor each solve problems in a specific application-space and cater to a wide spectrum of the standard simulation applications in science and engineering.

Due to complexities surrounding the effective integration of a static analog mesh com-

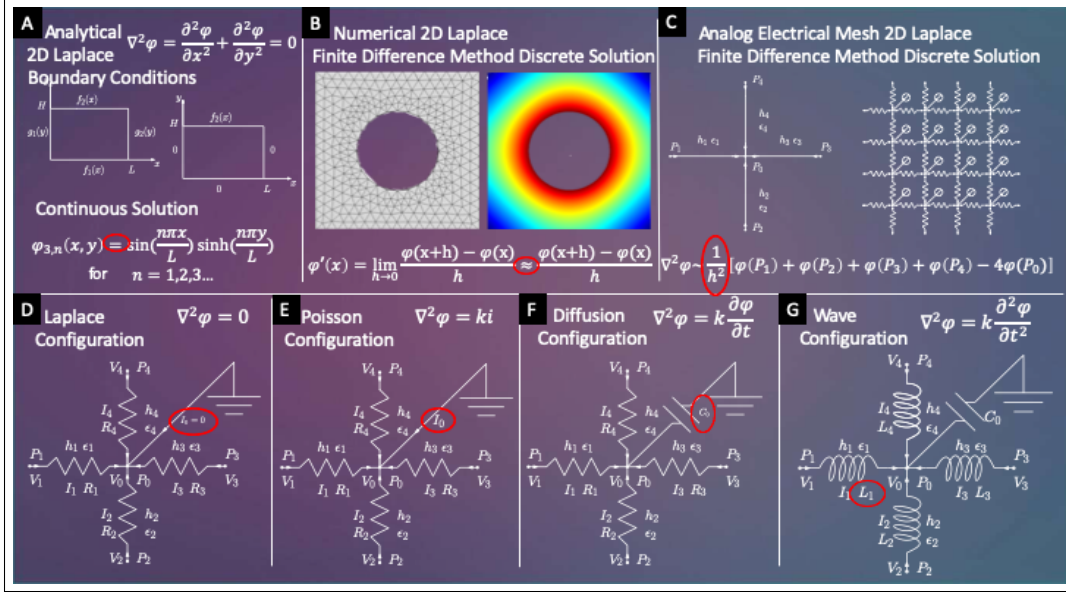


Figure 1.1: The top row of this figure illustrates the traditional options available for solving a PDE through (A) analytical, (B) numerical, and (C) analog electrical PDE solving paradigms, while the bottom row illustrates the reconfigurations of an analog electrical discrete solution for different classes of partial differential equation (PDE)s including (D) Laplace, (E) Poisson, (F) diffusion, and (G) wave equation.

puter in a Very Large Scale Integration (VLSI) architecture, the resistance network analogue has remained in the academic domain [21]. This shortcoming was improved upon by Ramirez-Angulo and DeYong [21] with a VLSI-friendly implementation of an analog mesh computer using Complementary Metal Oxide Semiconductor (CMOS) transistors operated in the subthreshold regime. However, modern digital VLSI designs prefer the use of minimum-size devices, which is at odds with subthreshold CMOS designs, which require larger devices to ensure proper matching [22].

Recent programs advocating for new and innovative computer architectures [23], and the recent introduction of innovative, programmable VLSI devices, such as the nanophotonic modulator [24], have created opportunities for innovative architectures that can take advantage of these new devices [25, 26]. Conceptual metastructure based analog computing models are starting to be developed by leaders in the field including Nader Engheta [27]. In the telecommunications space, Photonic ROC can potentially be used to efficiently model multiple-input and multiple-output (MIMO) systems that make substantial use of

PDEs [28]. The recent push for post-Moore computer architectures [23], has introduced a wide variety of application-specific accelerators [29, 30, 31]. Generally, these accelerators are designed to improve the performance of computationally-intensive algorithms by limiting unnecessary calculations or data movements. To maximize an application-specific computer’s utility, it must be capable of accelerating widely used algorithms. The progression to an analog electrical PDE solution accelerator is shown in Figure 1.1.

1.5 ROC Fundamentals

1.5.1 ROC

Reconfigurable Optical Computer (ROC) is a reconfigurable optical wavelength co-processor, implemented in two distinct physical technologies, capable of approximately solving PDEs through the finite difference method, constructed in a physical analog mesh but differing from the electrical implementation introduced in Figure 1.1 by performing summation of electrical density for Metatronic ROC and summation of optical intensity in Photonic ROC.

Increases in the RC time constant as a 2D electric mesh scales its number of nodes quadratically increases signal delay across the diameter of the mesh. If this signal delay exceeds the clock speed of the processor the computational time complexity of the analog electrical mesh degrades from $O(1)$ to $O(n)$ where n is the number of nodes along a single side of a square mesh.

Different electrical meshes, as shown in Figure 1.1, must be fabricated for different configurations of PDEs, therefore making an electronic analog static co-processor non reconfigurable.

Static photonic ROC utilizes changes in optical intensity due to optical loss to solve Laplace and Poisson PDEs. Metatronic ROC confines electric displacement current density $J_D = \frac{\partial D}{\partial t}$ in epsilon vary large (EVL) materials surrounded by epsilon near zero (ENZ) materials and directs J_D through nano-inductors, nano-capacitors, and nano-resistors.

The ability to change the accuracy of the PDE solution through the ratio of the density of the mesh versus the area of the PDE being solved for makes the ROC co-processor concept appropriate for future Energy-Quality (EQ) scalable systems, advocated for by green computing initiatives, which require the ability to explicitly trade off energy and quality at different levels of abstraction [32].

PDE & Physics	Edge Signal	Node Signal	Node "Potential"	Node Splitting Ratio
Laplace Electrical Lumped Element	Current [A] $I = V/R_{eff}$	Net Current [A] $\sum I_i$	Electrical Potential [V] $V = I_{net}R_{eff}$	Effective Resistance [Ω] $R_{eff} = R_1:R_2:R_3:R_4$
Laplace Photonic Distributed Circuit	Optical Intensity [Wm ⁻²] I_{int}	Net Optical Intensity [Wm ⁻²] (abstraction) $\sum I_{int i}$	Theoretical Optical "Node Potential"	Geometrically defined coupling & scattering
Laplace Metatronic Lumped Element	Electrical Displacement Current Density [Am ⁻²] $J_D = \frac{\partial D}{\partial t} = -j\epsilon\omega\vec{E}(\omega)$	Net Electric Displacement Current Density [Am ⁻²] $\sum J_{Di}$	Electric Displacement Field [Cm ⁻²] $\vec{D} = \epsilon\vec{E} = \epsilon\vec{E}_0e^{j\omega t}$	Effective displacement current density loss from $\text{Im}(\epsilon) \neq 0$

Figure 1.2: The Laplace PDE dependent physical units and equations for grid components in the electronic mesh, photonic ROC, and metatronic ROC are shown. The electrical and metatronic circuits operate as lumped elements and the photonic circuit operates as a distributed circuit. The equation units of metatronic ROC electric displacement current density are as follows: $\tilde{\epsilon}$ material permittivity [Fm⁻¹], $\omega = 2\pi f$ Angular Frequency [Hz], $E(\omega)$ electrical field [Vm⁻¹] or [NC⁻¹]. It is also important to distinguish between which photonic quantity's are measurable. We measure optical intensity through the use of a Y branch and a grating along each edge at the output of each optical node.

1.5.2 Photonic

Passive photonic ROC utilizes pure etched silicon waveguides and ring resonators combined with an central splitting element combined to form a photonic device that directs light evenly from the input port to the 3 output ports with a 33.3% 33.3% 33.4% splitting. Pho-

toinc ROC is fabricated within the GW clean room and is at a length scale greater than the wavelength of light, $\lambda = 1550 \text{ nm}$ being using. The distance form node to node is $h = 60 \text{ um}$. This size differential results in Photoinc ROC operating in accordance to the distributed element model shown in Figure 1.3.

Unfortunately there is a weak mapping of the electrical mesh to the photonic Mesh. This is because we must attempt to replicate electrical resistance with optical loss which is not equivalent. We also do not have a photonic equivalent to electrical capacitance or electrical inductance. However due to the relative ease of manufacturing a photonic mesh compared to a metatronic mesh we have invested energy and time into the photonic implementation of ROC as a way to demonstrate an initial fabrication. However the combination of equal splitting along with the distributed element model means that as we scale ROC for larger numbers of nodes the overall accuracy of the PDE solution decreases which is the opposite of what is desired for a analog finite difference algorithm as it is scaled up as noted in Figure 1.4.

1.5.3 Metatronic

In microelectronics and combination of an electrical current and electrical potential through lumped elements including resistors, inductors, and capacitors has led to successful modularization of circuit design through the radio frequency and microwave domains. As we have seen in the photonic case, operating in the optical domain while still benefiting from a lumped circuit paradigm is not trivial. As Nadar Engatar stated in his 2007 Science paper [33] there are two primary challenges to overcome. In lower frequency domains, designs involve elements that are much smaller than the wavelength of operation, fabrication techniques can be used to construct sub wavelength dimensions at optical wavelengths. Secondly the response of metals at IR and optical frequencies cannot be scaled directly from RF to optics.

The ideal metamaterial-based implementation of ROC with epsilon near zero set equal

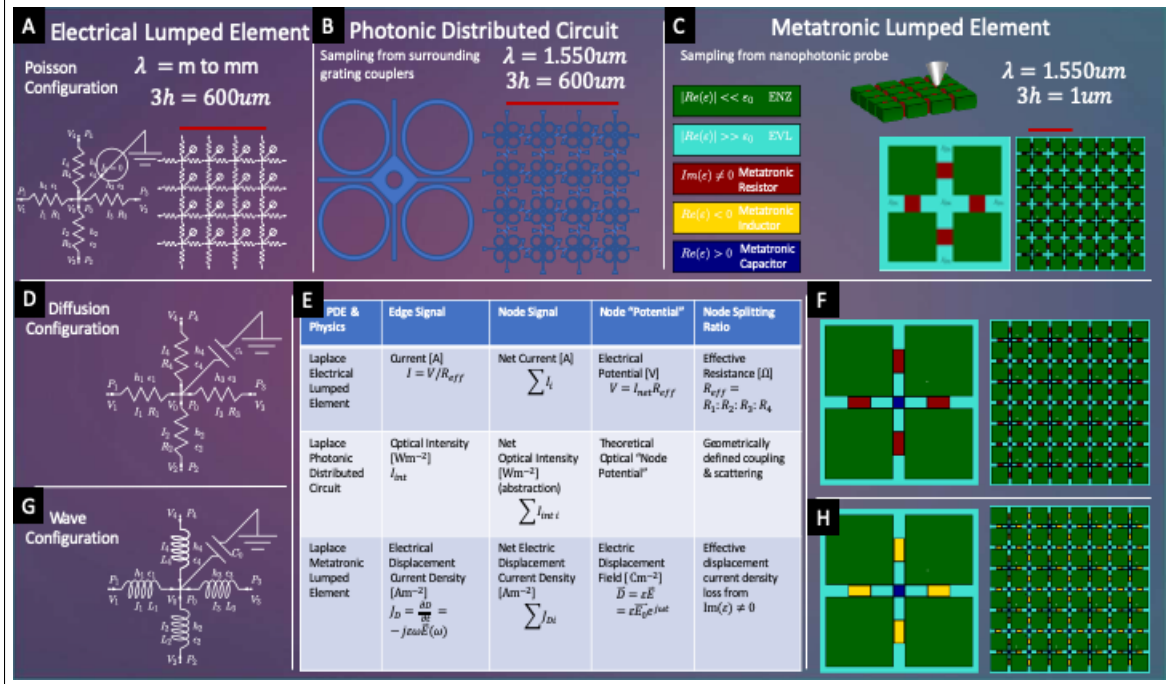


Figure 1.3: The top row of this figure illustrates the different analog grid based PDE solving technologies including (A) the original electrical analog, (B) the silicon photonics implementation, and (C) the Metatronic Implementation. The columns represent the different configurations of the grid, that give the “reconfigurable” optical computer its name, allowing for Poisson, diffusion, and wave configurations. As you probably have noticed, there is no photonic schematic showing an equivalence to (D) electrical capacitance, or (G) electrical inductance, but there is (F) metatronic capacitance and (H) metatronic inductance. Table (E) shows the physical effects utilized in the technologies and is shown in larger form in Figure 1.2. In the language of graph theory, a node is a grid point within the mesh, and an edge is a connection between grid points.

to zero as well as physically possible epsilon near zero values are simulated in the COMPSOL Multiphysics based metatronic solution. of ROC. Upper bounds are placed on the accuracy by λ/L , where L is the feature size of the network components, due to the physical nature of light, and λ is the wavelength.

Metatronics enable the ideal ROC implementation, in terms of size and accuracy. However, the complexities of an effective integration of a high speed programmable and concurrently energy efficient static-like analog mesh significantly reduced the advancement of this technology. Here, we demonstrate the implementation of a nano-optic co-processor able to solve partial differential equation based on a metatronic nanocircuit board.

Thanks to a unprecedented control of the epsilon-near-zero (ENZ) and material losses over Indium tin oxide (ITO), we use different deposition conditions, in order to tune the ENZ position, which potentially leads to a top-down monolithically integrated circuit [34]. The elements of the circuit could be then be electrostatically tuned [35, 36, 37, 38] and reprogrammable aiming to solve a variety of PDEs including Poisson, diffusion, and wave.

A discussion on losses and physical limitation, induced by the losses of the ITO at ENZ condition is provided. The solution accuracy and its scaling functions are estimated for to finite difference approaches, and compared to other mesh solutions. The implementation of an all optical read-out paradigm is discussed based on a Nanophotonic probe card that detects the local near field of the scattered field and provides information of a dielectric displacement, at given points of the nano-optics circuit, thus allowing to extrapolate the results of the computation.

1.6 Accuracy

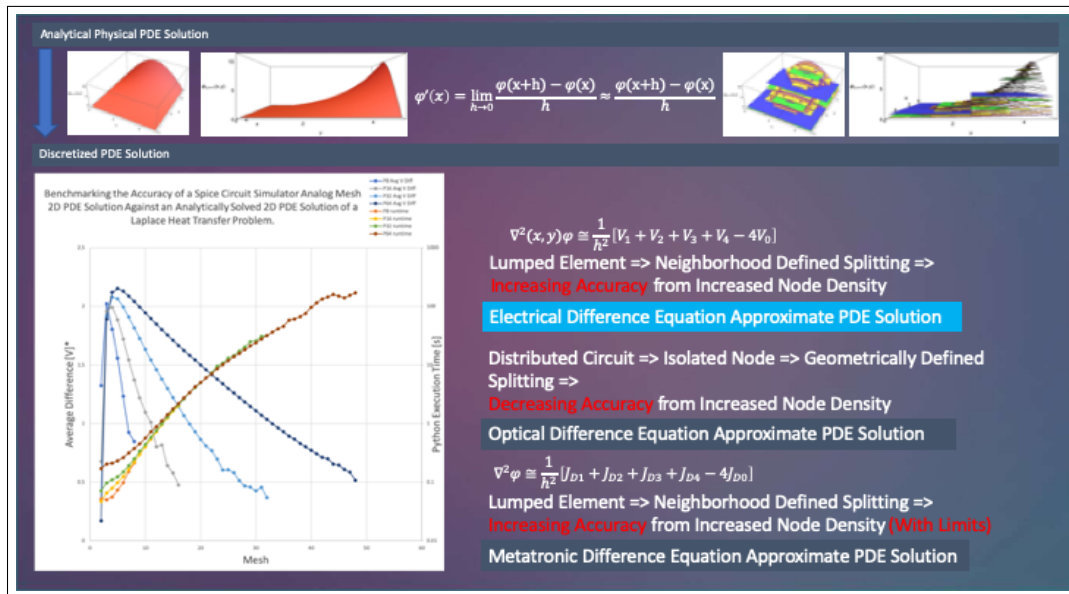


Figure 1.4: Electronic analog exhibits lumped element, neighborhood defined splitting, and increased accuracy from increased node density.

When transitioning from analytical to discrete Solutions, discretization error is the prin-

cipal source of error in the finite difference method employed in all of the discrete information processing techniques that are discussed in the thesis. For a one dimensional problem the discretization error of ψ can be defined in terms of its derivative. This spatial change is defined by h , and shown at the top of Figure 1.4, which is finitely small and the removal of the limit creates the approximation which is defined as the discretization error. For a dense discretized solution where the number of nodes n approaches infinity and acts like a continuous solution we expect the accuracy of the overall solution to increase. One can see accuracy improvement electronically as the electronic analog exhibits lumped element, neighborhood defined splitting, and increased accuracy from increased node density as shown in Figure 1.4.

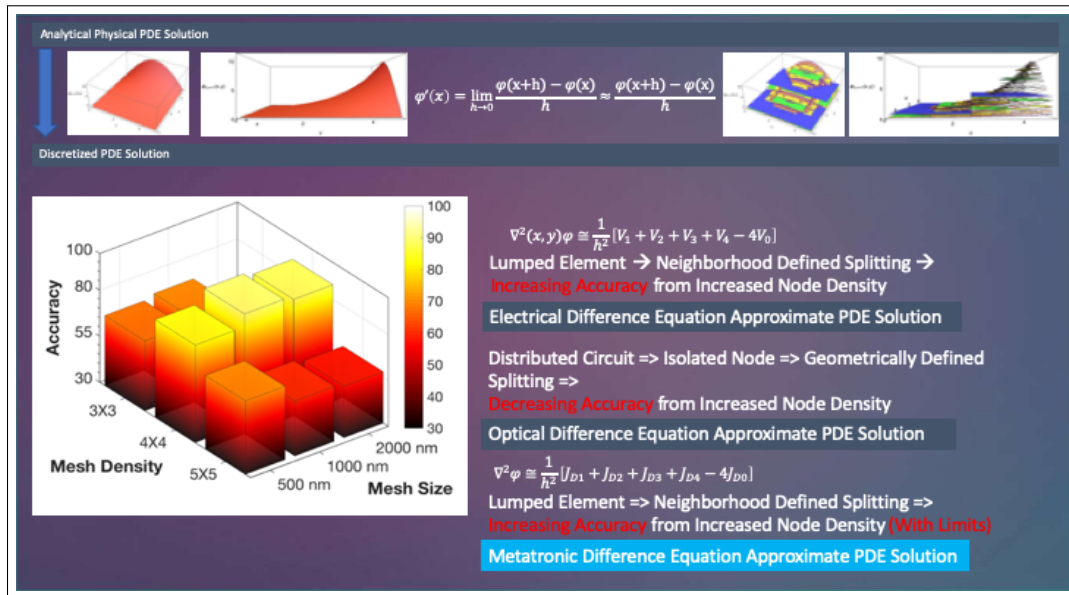


Figure 1.5: The metatronic circuit exhibits lumped element, neighborhood defined splitting, and therefore increasing accuracy from increased node density all at a smaller operational wavelength than the electrical analog.

The details of geometric optical splitting utilized in the photonics mesh is explored by my colleagues Shuai Sun and Engin Kayraklioglu who will give a deep explanation in their dissertations. However due to the distributed circuit, isolated node, and therefore geometrically defined splitting behavior, phonically one expects decreasing accuracy from increased node density. This does not mean that a photonic implementation cannot provide a useful

approximate solution, but the photonic architecture needs to compensate for this negative effect. On a positive note, the metatronic circuit exhibits lumped element, neighborhood defined splitting and therefore increasing accuracy from increased node density all at a smaller wavelength than the electrical analog as shown in Figure 1.5.

Chapter 2 - Mathematics & Physics Underlying the Computational Model

2.1 Computational Time Complexity Requirements

The two dimensional implementation of the electrical, photonic, or metatronic analog approximate PDE solving algorithm needs to operate as close to $O(1)$ constant time as possible in order to provide a useful analog advantage. Figure 2.1 indicates the number of sources and samples needed as well as the limits of mesh dimensions in order to stay in constant time, and therefore potentially be incorporated as an analog accelerator into, as an example, the commonly used digital parallelized multi-grid method operating at a logarithmic $\Theta(\log x)$, polylogarithmic $\Theta(\log^2 x)$, or fractional Power $\Theta(\sqrt{x})$ time complexity, depending on course fine grid traversal for a grid with x grid points.

2.2 Analytical Derivation PDE Solution

2.2.1 Analytical Solution

Laplace's equation is a second-order partial differential equation which produces, as a solution, harmonic functions that accurately describe the behavior of electric, gravitational and fluid potentials. It has no time dependence, only a spatial dependence, and is often written as

$$\nabla^2 \varphi = 0 \tag{2.1}$$

where ∇^2 is the Laplace operator and φ is a scalar function.

For the purpose of simplicity, we will only discuss spatial variables x and y , which allows Laplace's equation to be rewritten as

$$\frac{\partial^2 \varphi}{\partial x^2} + \frac{\partial^2 \varphi}{\partial y^2} = 0 \tag{2.2}$$

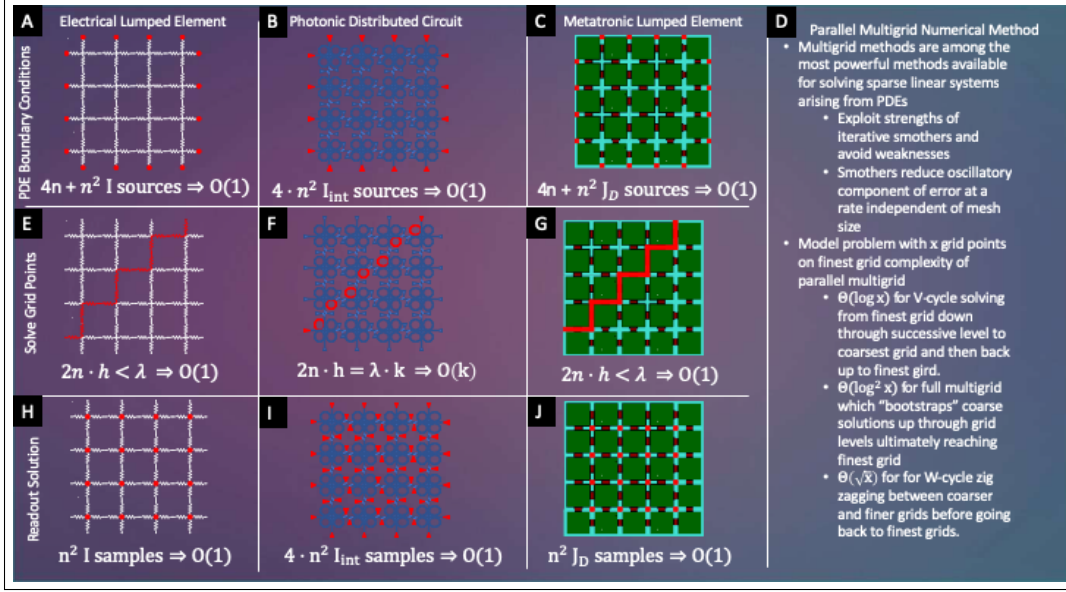


Figure 2.1: Computation time complexity of a single PDE analog grid solution iteration in the three analog physics technologies could be incorporated into a **(D)** parallelized multi grid method using finite difference method operating at logarithmic time, polylogarithmic time, or fractional power time depending on the course fine grid traversal utilized. For one of the analog system to remain in the constant time domain certain hardware requirements must be met. If we assume that n is the number of nodes in a one dimension side of an grid and h is the length of an edge between nodes in the grid, we can see that the number of **(A)** current, **(B)** optical intensity, and **(C)** displacement current density hardware source locations are needed to set boundary conditions, shown on the top row, and we can see the needed number of **(H)** current, **(I)** optical intensity, and **(J)** displacement current density sample locations are required to read out a PDE analog solution. With all of these sources and samples operating in parallel. The grid length scales for the **(E)** electrical **(G)** metatronic execution step remain within one operation wavelength for both technologies, and thus remain in constant time, where as the **(F)** photonic grid length scale exceeds its operational wavelength, and thus requires k iterations to traverse the diameter of the grid

Following the derivation in section 2.7.1 [39] results in the product solutions yielded by the separation of variables method up to a constant.

$$\varphi_{3,n}(x, y) = \sin\left(\frac{n\pi x}{L}\right) \sinh\left(\frac{n\pi y}{L}\right) \quad \text{for } n = 1, 2, 3, \dots \quad (2.3)$$

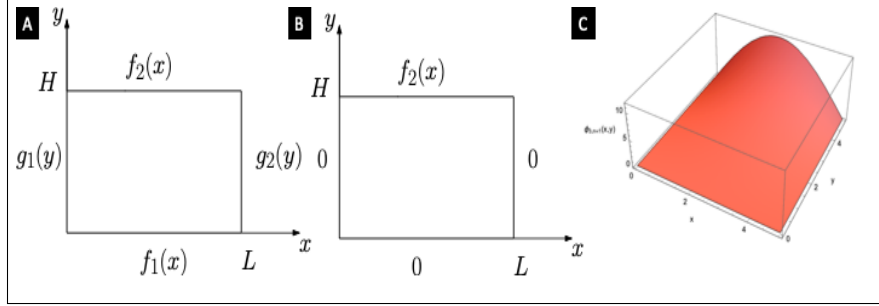


Figure 2.2: **(A)** The four boundaries of $\psi(x, y)$ are defined in terms of the x and y axis. **(B)** The one non-zero boundary condition and three zero boundary conditions for the $\varphi_3(x, y)$ solution component of $\varphi(x, y)$. **(C)** Plot of $\psi_{3,n}(x, y)$ with $n = 1$, $L = 5$ and $H = 5$ with the continuous solution shown in the z axis.

2.2.2 Physical Units

Why is necessary to discuss the physical interpretation of the purely mathematical solution of the Laplacian partial differential equation? To better understand the source of inaccuracies that deviate from the analytical solution derived in Section 2.2.1 caused by discretization and the implementation of different analog algorithms built on physical hardware we must first address the inequality of units associated with the generated solutions. The analytical solution is purely mathematical and therefore unitless. The digitally generated discretized numerical solution outputs heat map in Kelvin [K]. The electrical analog algorithm mesh can sample solutions either in Volts [V] or current [A]. Photonic ROC outputs solutions in Optical Intensity [Wm^{-2}]. Metatronic ROC outputs solutions in Electric Displacement Current Density J_D [Am^{-2}].

Initially we have been normalizing all our solutions between zero and one. However to determine true equivalence in the future we can potentially add physics to our analytical solution and generate a solution for a temperature distribution in Kelvin [K]. By mapping electrical, photonic ROC, and metatronic ROC to an equivalent temperature distribution in Kelvin, we can remove unit mismatch as a source of inaccuracy.

2.3 Discrete Numerical PDE Solution

2.3.1 Numerical Solution

When using COMSOL Multiphysics to solve a two dimensional heat transfer PDE the user of the software must define the boundary conditions of the problem and specify the flux at each of those boundary conditions. This process is relatively similar to the analytical method described in Section 2.3. The process deviates when the user must specify the computational mesh element size and the geometry of the mesh showed in Figure 2.3. It should be noted that all computations performed in the thesis have access to the same computing resources described in Section B.1.1.

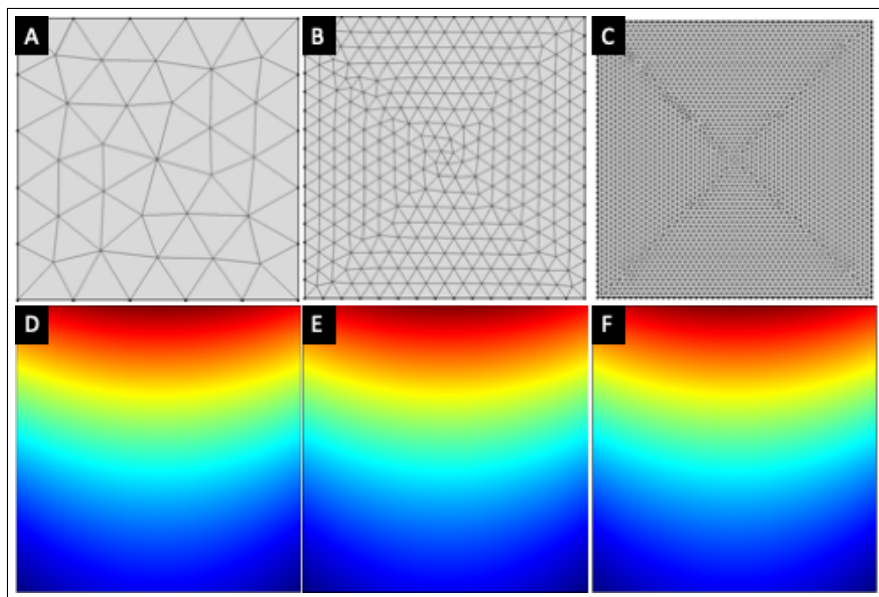


Figure 2.3: The finalized COMSOL geometry has one domain, 4 boundaries, and 4 vertices. **(A)** The physics controlled normal element size mesh consists of 68 domain elements and 20 boundary elements, **(B)** 578 domain elements and 60 boundary elements, and **(C)** 6282 domain elements and 200 boundary elements. The number of degrees of freedom solved for is **(D)** 157 plus 44 internal DOFs and the solution is solved for in 1 seconds, **(E)** DOFs 1217 plus 124 internal DOFs solved for in 2 seconds, and **(F)** DOFs 12765 plus 404 internal DOFs solved for in 1 second.

The COMSOL Multiphysics numerical heat transfer PDE solutions are used to benchmark the accuracy of the analog algorithm implementations described in Section 2.4, Sec-

tion 2.5, and Section 2.6 because all 4 solutions include discretization error, described in Section 2.3.2, that deviates from the continuous analytical solution in Section 2.2. When striving to showcase the advantages of the analog algorithms, it is important to consider that the numerical solution benefits from the advantage of optimization of mesh geometry, shown in Figure 2.3, whereas the analog implementations have fixed rectangular meshes. The general lack of flexibility of analog implementations is one of these primary weaknesses, and what I try to compensate through reconfigurability.

2.3.2 Discretization Error

In applied mathematics, discretization is the process of transferring continuous functions, models, variables, and equations into discrete counterparts. The discretization error is the error resulting from the fact that a function of a continuous variable is represented by a finite number of evaluations, in this case on a lattice. This visualization code for the discretization of our non physical analytical solution through the use of mesh scaling along a power law with exponent of 2 can found at ROC discrete visualization. The discretization scaling is shown in figure 2.4.

Discretization error is the principal source of error in the finite difference method employed in all of the information processing techniques this paper discusses. For a one dimensional problem the discretization error of $\varphi(x)$ can be defined in terms of its derivative

$$\varphi'(x) = \lim_{h \rightarrow 0} \frac{f(x+h) - f(x)}{h} \approx \frac{f(x+h) - f(x)}{h} \quad (2.4)$$

where h is finitely small and the removal of the limit creates the approximation which is defined as the discretization error. For a dense discretized solutions where the number of nodes n approaches the limit ($2^n \Rightarrow 2^\infty$) and acts like a continuous solution allows us to quantify the amount of inaccuracy generated by the discretization process and therefor better understand the effects of the physical properties of the electrical, optical, and meta-

tronic information processing on their achievable accuracy's by accounting for inaccuracies caused by discretization which exists in all analog algorithm implementations.

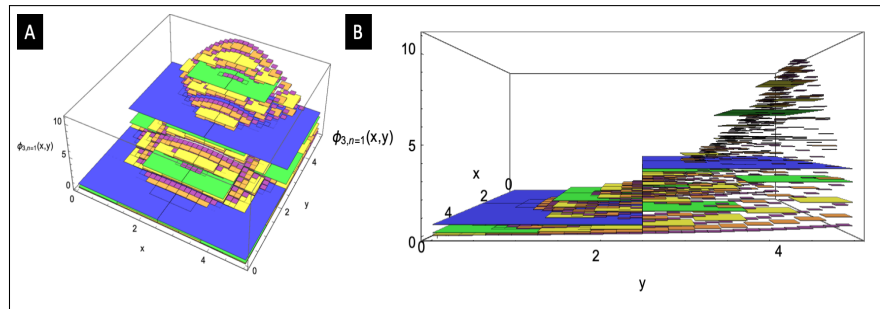


Figure 2.4: **(A)** Plot of $\psi_{3,n}(x, y)$ with $L = 5$ and $H = 5$ with the the discretized mesh $2^1 = 2$ blue, $2^2 = 4$ green, $2^3 = 8$ yellow, $2^4 = 16$ orange, and $2^5 = 32$ purple solutions shown in the z axis. **(B)** The right side view is shown.

2.4 Electrical Analog PDE Solution

2.4.1 Electrical Elements

An electrical mesh analog finite difference algorithm utilizes basic circuit elements including capacitance (C), inductance (L), and resistance (R), from which more complex subsystems such RLC circuits can be designed. Redshaw and Liebmann designed an apparatus which uses the relaxation technique to solve PDEs describing oscillatory flow [20] and heat transfer problems [6] using a resistive mesh. This device, called a resistance network analogue, is comprised of resistors connected in a two-dimensional mesh configuration. Finite difference mesh points characterize the stencil for a specific PDE, and are mapped to a resistive mesh for calculation. Solutions are read at the intersection of resistor terminals, or nodes, as shown in Figure 2.5.

This illustrates the resistance network analogue's ability to solve for a PDE using a voltage derived from current summation at each node. Monitoring of the voltage at each node yields a solution for each element in the computational mesh.

Liebmann showed the error introduced by voltage and current measurements to be negligible, thus reducing the factors which limit the accuracy of the resistance network

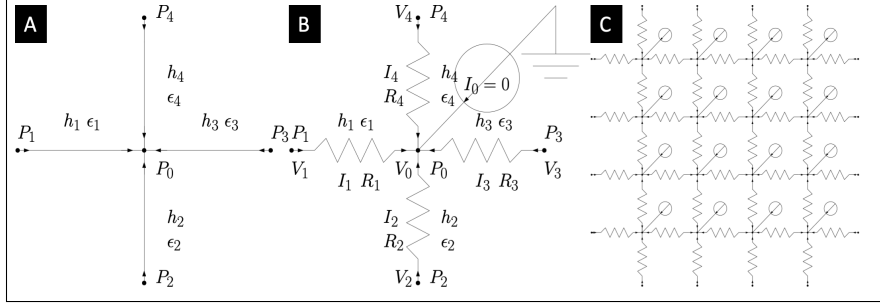


Figure 2.5: **(A)** The derivative of the function φ at point P_0 is expressed through the differences of φ between points P_0 and $P_1, P_2, P_3,$ and P_4 . The distance between P_0 and P_1 is labeled h_1 . The scalar function ϵ for vector function φ between points P_0 and $P_1, P_2, P_3,$ and P_4 is labeled ϵ_1 between P_0 and P_1 . **(B)** The voltage $V[V]$ at point P_0 is expressed as V_0 . The current $I[A]$ and Resistance $R[\Omega]$ between points P_0 and P_1 is expressed as I_1 and R_1 respectively. The same naming conventions apply for $P_2, P_3,$ and P_4 . I_0 is the input current and R_0 is defined in terms of other resistances, and therefor not shown on the diagram. **(C)** Poisson class electrical 16 node resistance network with the ability to apply a current at each node.

analogue to simply the mesh size and tolerance of components comprising the mesh [6]. Principles that govern the relaxation technique state that the mesh size must be made so small that the replacement of the PDE by the finite difference equation is permissible, and that any error introduced by a mismatch in mesh size and resolution requirement can be corrected with a correction function [6]. Liebmann also showed that such a network of resistors contains averaging properties which minimize the error introduced by tolerances in individual resistor values [6].

2.4.2 Difference Equation Approximation

$$\nabla \cdot \epsilon \nabla \varphi = g \tag{2.5}$$

The use of an electrical mesh allows us to generate the solution of an approximation of the partial differential equation 2.31 referred to from here on as the electrical difference equation solution. In the partial difference equation 2.31 where ϵ is the known scalar function, φ is the function, and $g = 0$ is the function relationship for a time independent

Laplace second order partial differential equation. By defining an electrical mesh as shown in Figure 2.5 and scaling the mesh we can performing linear interpolation as shown fully in Section 2.7.2 and by disregarding the higher order terms we say that Equation 2.5 is asymptotically equal to

$$\nabla^2\varphi \simeq \frac{1}{h^2} \left[\varphi(P_1) + \varphi(P_2) + \varphi(P_3) + \varphi(P_4) - 4\varphi(P_0) \right] \quad (2.6)$$

which is equal to

$$\nabla^2\varphi \simeq \frac{1}{h^2} \left[V_1 + V_2 + V_3 + V_4 - 4V_0 \right] \quad (2.7)$$

The solution to the function φ in the differential equation Equation 2.5 has been approximated through the use of a difference equation. The solution is attained through measurement of voltage values at grid points. All that remains is to set the required boundary conditions to obtain the full solution if $g \equiv 0$ everywhere. If $g \neq 0$ currents from Equation 2.39 have to be fed into mesh points. The resistance network performs the "relaxation technique" automatically and instantaneously for a Laplace equation.

The accuracy of the electrical mesh pde solution is shown to increase with an increase in mesh density and be independent of the problem area size solved for between pde problem sizes 8,16,32, and 64, indicated by the reduction in the absolute (non normalized) difference between the generated electrical mesh solution script, accessible (although currently in private repository) via Section A.1, and the analytical solution described in Section 2.2, and derived in Section 2.7.1, shown in Figure 2.6. We also see that the simulation time required for the Spice circuit simulator increases exponentially for increased mesh density.

It is important to note that we do not have an estimate concerning the scaling of execution time of the physical electrical mesh, as we have not fabricated one, however I believe it would showcase the fundamental speedup discussed in Section 2.1. Figure 2.6 behaves in accordance with our understanding of the effects of finite difference error reduction de-

scribed in Section 2.3.2.

2.5 Photonic Analog PDE Solution

Silicon Photonics supports weighted summation through constructive and destructive interference of waveguide confined light, can be assembled into a grid/mesh structure with nodes that route light, and light sources and light detectors that are able to set boundary conditions and readout solutions. Due to these similarities it is tempting to assume an equivalence exists between the Electrical Mesh introduced in Section 2.4, however we will show that there are fundamental physical differences between how the Photonic node behaves compared to the electrical node. Despite these differences Silicon Photonics has established fabrication procedures both internally at the Orthogonal Physics Enabled Nanophotonics (OPEN) Lab and GW Nanofabrication and Imaging Center (NIC) as well as externally at commercial foundries including the American Institute for Manufacturing Integrated Photonics (AIM Photonics). The physics of Metatronic ROC discussed in Section 2.6 encompass a better mapping to the Electrical Difference equation in Section 2.4 but current Metatronic fabrication processes are in their infancy and are currently done at length scales [40] orders of magnitude greater than what is needed for our Nanoscale Metatronic ROC implementation. The combination of imperfect mapping and feasible fabrication make Photonic ROC worthy of understanding and implementing as a way to showcase current capabilities of optical analog computing.

2.5.1 Limitations of Passive Photonic Difference Equation Approximation

Photonic ROC operates in the optical band at $\lambda = 1550$ nm with waveguide and optical splitter dimensions in length scale order of micrometers, far larger than the operating wavelength of light, resulting in distributed element model characteristics for the optical circuit. Current fabricated Photonic ROC is passive with a future active Photonic ROC planned to be fabricated at AIM Photonics.

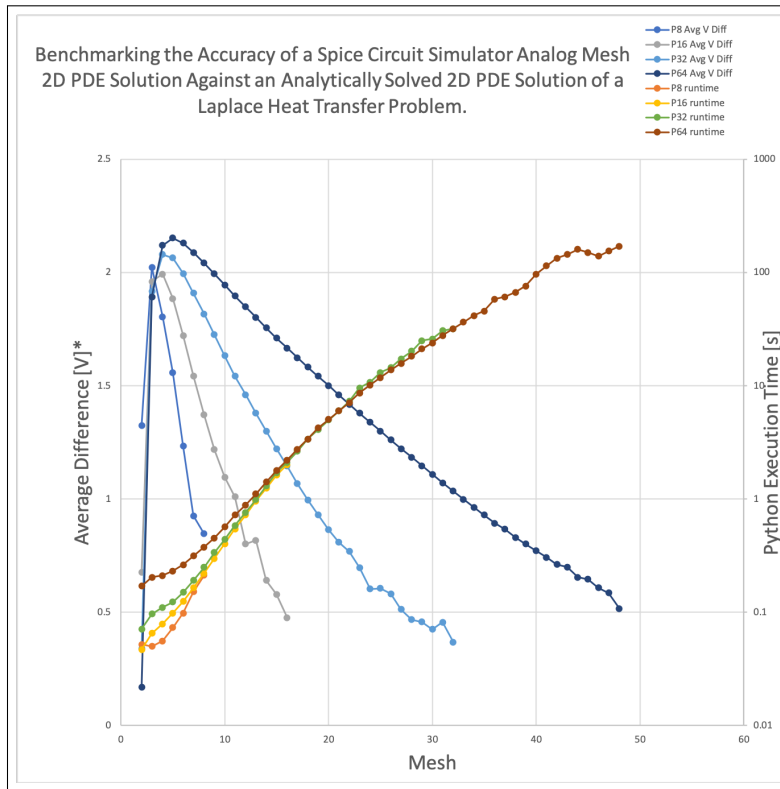


Figure 2.6: Benchmarking the accuracy of a spice circuit simulator analog mesh 2D PDE solution against an analytically solved 2D PDE solution of a Laplace heat transfer problem. Mesh based solutions are scaled linearly from 2 up to the problem size N with problem sizes 8, 16, 32, and 64 plotted. Average difference is calculated by comparing the spice based voltage value at a mesh point coordinate to the value sampled from the continuous analytical solution at the same coordinate. Then the difference from all Simulation Program with Integrated Circuit Emphasis (SPICE) analytical coordinate comparisons in a mesh are averaged, resulting in a single average difference point which is plotted for each mesh for each problem size. This average difference is the measure of accuracy with a higher difference resulting from a greater deviation in the spice solution from the "true north" analytical solution. Thus a lower average difference implies a higher accuracy with a value of 0 being a perfect match. *Analytical solutions not scaled for volts yet. *Program crashed at Mesh 49 on problem 64.

Initial experimental fabrications of Photonic ROC have been composed of pure silicon and have been passive optical circuits, meaning that waveguide geometry is the driving force for circuit behaviour.

Although there is no photonic equivalent of electrical inductance or capacitance at micrometer length scales, optical loss due to waveguide attenuation can be considered analogous to electrical current resistance. The fixed optical loss fabricated into waveguide geometries allows for passive photonic ROC to approximately solve Laplace class PDEs.

Unlike the electrical mesh, each Photonic ROC splitting node, composed of 4 ring resonators and a central splitter, due to its micrometer size and distributed element model behavior is effectively isolated from its neighborhood of surrounding nodes due to the limit of what a single wavelength of light can reach in a discrete time step.

Computationally this means that at a single point in time the only physical effect that determines how much light is sent into each of three possible waveguides or is reflected back into the originating waveguide is the geometry of the node which is fixed. Irregardless of boundary conditions set and inbound light from surrounding waveguides, each optical node will always split light in the same percentages, determined by its geometry. This physics is fundamentally different from the splitting occurring in the electrical mesh in Section 2.4 and Metatronic ROC in Section 2.6 in which each node's "visibility", due to their lumped circuit behavior, operates as an all to all network at any given time step. In a finite difference algorithm that relies on a nodes immediate neighborhood to calculate the measured value at a node, the neighborhood visibility of a single node is paramount. The effects of the photonic splitting paradigm will be explored but first it is important to understand the path that light travels through a node.

As light enters the node a percentage is coupled into the left and right ring resonators on either side of the waveguide prior to entering the central square where the light is reflected off of the central circular cavity with an eventual archived splitting of roughly 33% of the light traveling into each of the three surrounding waveguides as shown in Figure 2.7. The

design process, physics, and geometry of this novel splitter will be covered in depth in the dissertation and future Photonic ROC fabrication paper of PhD candidate and OPEN Lab member Shuai Sun.

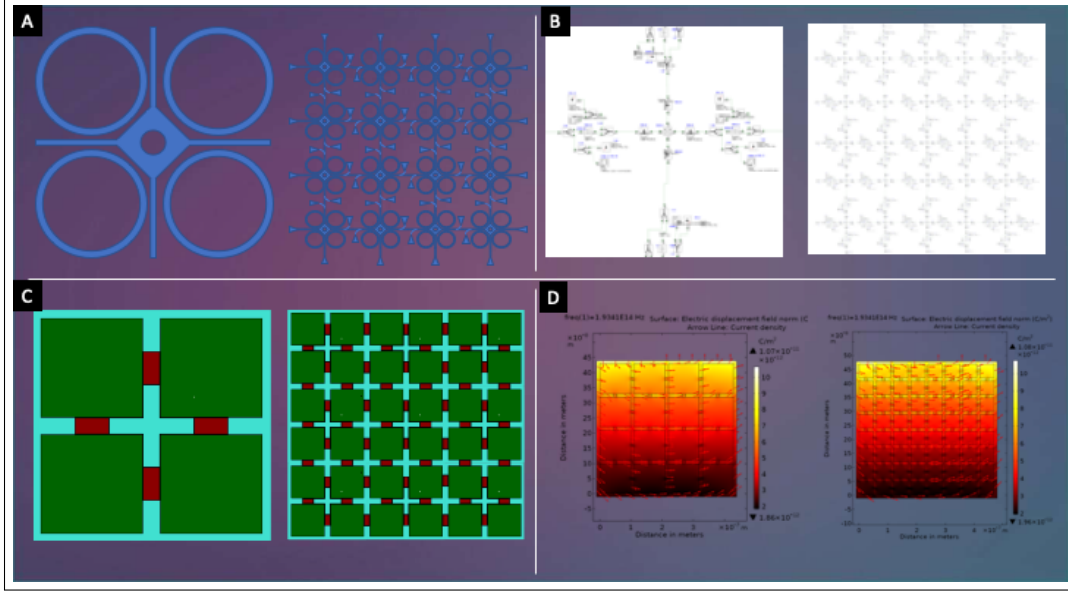


Figure 2.7: The (A) geometrically engineered fixed optical loss fabricated into waveguide geometries allows for (B) Lumerical INTERCONNECT passive photonic ROC simulations to approximately solve Laplace class PDEs. However, unlike the electrical mesh, each photonic ROC splitting node, composed of 4 ring resonators and a central splitter, due to its micrometer size and distributed element model behavior is effectively isolated from its neighborhood of surrounding nodes due to the limit of what a single wavelength of light can reach in a discrete time step. The (C) metatronic splitting is neighborhood defined and can be (D) simulated with COMSOL to showcase the ENZ confinement of displacement current density.

The difference equation mapping for Photonic ROC is the same as the electrical mesh up to Equation 2.33. Once Physics becomes involved in the mapping, the first step is for current summation from the electric mesh described in Equation 2.36 to roughly map the optical intensity measured by the sum of the output grating couplers attached to each output waveguides of each splitters written as

$$\sum_{n=1}^4 P_n = 0 \quad (2.8)$$

where P_n is the optical intensity measured at each of the output grating couplers of each node.

2.6 Metatronic Analog PDE Solution

2.6.1 Device Physics

When transitioning from the traditional static electrical resistor mesh operating in radio frequency from ($f \simeq 30$ Hz, $\lambda \simeq 10\,000$ km) to ($f \simeq 300$ GHz, $\lambda \simeq 1$ mm), or microwave frequency from ($f \simeq 300$ MHz, $\lambda \simeq 1$ m) to ($f \simeq 300$ GHz, $\lambda \simeq 1$ mm) described in Section 2.4 to the Metatronic subwavelength optical frequency domain of ($f \simeq 193$ THz, $\lambda \simeq 1550$ nm) described in Section 2.6, control voltage, V , in each electrical node is substituted for electric field, E in each Metatronic node. Thus metatronic ‘current’ is not given by the conductivity, but by the displacement current density, $J_D = \frac{\partial D}{\partial t}$, where D is the electric displacement [41].

The Metatronic circuit board needs to adhere to the condition that J_D is not flowing outside the ‘wire’. This can be realized via biasing a waveguide board to the epsilon-near-zero (ENZ) point, where $\text{Re}(\varepsilon) = \text{real part of permittivity} = 0$ (or near zero). Here the ‘wire’ is given by regions where $\text{Re}(\varepsilon) \gg 0$, termed epsilon very large (EVL), where J_D is conducted.

In order for the metatronic circuit mesh to accurately map to the finite difference equation the physical mesh dimension, d , must be much smaller than the optical operation wavelength, $\lambda = 1550$ nm (i.e. $d \ll 1550$ nm) in order to create the lumped element condition.

In order to duplicate the electrical circuit components resistors, inductors, and capacitors in the metatronic optical subwavelength domain, and in doing so reconfigure the mesh for diffusion and wave equations, the circuit must take advantage of the materials permittivity properties. If the material is a conventional dielectric (e.g., SiO₂ or Si) with $\text{Re}(\varepsilon) > 0$ at optical frequencies, the nanoparticle will act as a capacitive impedance (i.e., nano capacitor). If the particle is made of material with $\text{Re}(\varepsilon) < 0$ at optical frequencies (e.g., noble metals such as Ag and Au), the particle may behave as a negatively capacitive impedance,

which implies that it will behave as an inductive impedance (i.e., nano inductor). When the material exhibits some material loss, that is when $\text{Im}(\varepsilon) \neq 0$ (which is almost always the case), a "nano resistor" element should be included in the nanocircuit [33].

The ENZ materials used is Indium tin oxide (ITO) with electrical properties shown in Figure 2.10. The Drude model applied to ITO allows one to define optical equivalent circuit models provided the size of the mesh.

2.6.2 Finite Difference Equation Equivalence

Following the difference equation mapping in Section 2.7.2 through Equation 2.34 and by sampling displacement current density at each node as well as the node's immediate neighborhood of nodes one edge away, we produce an asymptotically equivalent equation to partial differential equation 2.5 for each Metatronic mesh grid point

$$\nabla^2 \varphi \simeq \frac{1}{h^2} \left[J_{D1} + J_{D2} + J_{D3} + J_{D4} - 4(J_{D0}) \right]. \quad (2.9)$$

Equation 2.9 is similar to the application of Kirchhoff's law to the currents $\varphi(P_i)$ meeting at the junction O of a lumped circuit mesh described in Equation 2.7.

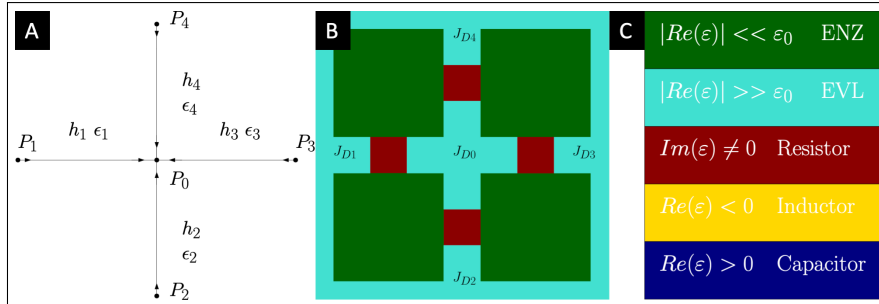


Figure 2.8: The figure shows a (A) finite difference node, a (B) metatronic resistive node with displacement current density sampling locations, and a (C) metatronic material relative permittivity reconfigurability key.

An equivalent metatronic nano-optic node is presented in Fig 2.8. We exploit the concept that nanoparticles (NPs) in the optics domain can be treated as lumped circuit elements, whose impedance is defined in terms of the perturbation to the displacement current, J_D in

response of the electric field E . The materials complex permittivity $\tilde{\epsilon}$ acts as a variable for displacement current as follows

$$J_D = \frac{\partial D}{\partial t} = -j\tilde{\epsilon}\omega E(\omega). \quad (2.10)$$

which, for element size considerably smaller than the optical wavelength [Engheta], represents an equivalent Ohm's law in the optical domain, enabling the mapping of the resistive circuit. In order to convey the flux of the displacement current a sub-wavelength circuit is considered to be carved in an epsilon-near-zero substrate, which for specific optical bandwidth enables light to travel through the grooves just like current in copper wiring [42].

Resistors, capacitors and inductors can be modelled as portions within the air grooves, with materials with well defined permittivity values. In order to map equation 2.37 in the metatronics circuit, the resistors are modelled as a dissipative dielectric where $R = -j\omega\tilde{\epsilon}$ if $\tilde{\epsilon}$ is a complex number.

Due to the confinement of the displacement current in the air grooves, the impedances are locally coupled, which in terms of electrical circuit means that a Norton/Thevenin equivalents are admissible. Therefore, for a limited functional bandwidth, for which the material of the board is in ENZ condition, Kirchoff's law at the mesh is satisfied, providing identical results with respect to a resistive network, reported in Equation 2.9.

2.6.3 Solution of Laplace Equation

By following the analytical derivation in Section 2.7.1 and the electrical mesh mapping in Section 2.7.2 as a starting point from which we utilize COMSOL Multiphysics to simulate the electric field displacement and the displacement current in a 3x3 metatronics mesh. A strong local electric field, generated by an horizontal dipole, is used for representing the heat source, while ENZ condition is applied to the rest of the boundaries. In this section, as an illustrative and not limiting, example the permittivity of the circuit board is

considered to have negligible losses ($\epsilon'' < 0.1$) ($\tilde{\epsilon} \simeq 0$) with an overall size of 1000 nm ($d < \lambda$) [43, 44].

The overall dimension of the circuit of Fig. 2.7C is supposed to be smaller than the operating wavelength, as required for conventional electronic circuit concepts at low frequencies. However, the “spatially static-like” properties of the ENZ substrate, i.e. absence of a significant phase variation in ENZ, essentially relax this requirement for the optical nano-circuit board of Fig. 2.9, for which the total length may become also several free-space wavelengths long (while it is electrically small compared to the very long wavelength in ENZ).[44]

Under these conditions, the field lines in Figure 2.9 highlights that the Electric displacement and consequently the displacement current, fall only within the air grooves, forced by the ENZ conditions in the neighboring area ($D \simeq 0$).

These COMSOL Multiphysics simulations, with maximum computational mesh size of 5 nm, of electric displacement field, with $\lambda \approx 1550$ nm and $f \approx 193$ THz, over Indium tin oxide (ITO), with complex permittivity $\epsilon = 1.0e - 4 + i0.3$, in epsilon-near-zero (ENZ) condition squares in subwavelength optical regime surrounded by air channels, with a width of 10 nm, broken by metatronic resistive $10 \text{ nm} \times 10 \text{ nm}$ squares composed of ITO with complex permittivity $\epsilon = 1.0e - 4 + i0.3$ squares described in section 2.6.1. The simulation applies an initial electrical field along the top of each array with a value of 1 V m with scattering boundary conditions applied to the remaining three sides of each array. The electrical displacement current density (shown as white arrows), used to sample the PDE solution from the grid, is confined to the air groves surrounding and throughout the mesh.

Solutions of the PDE solving metatronic processor with increasing mesh density are reported in Figure 2.11. Interestingly, the solution given by the metatronic circuit for increasing mesh densities, keeping the overall circuit dimension, maps precisely the solution of a finer mesh in a finite difference approach. This is can be achieved only if the circuit board is characterized by negligible losses, which causes the absence of a dielectric field

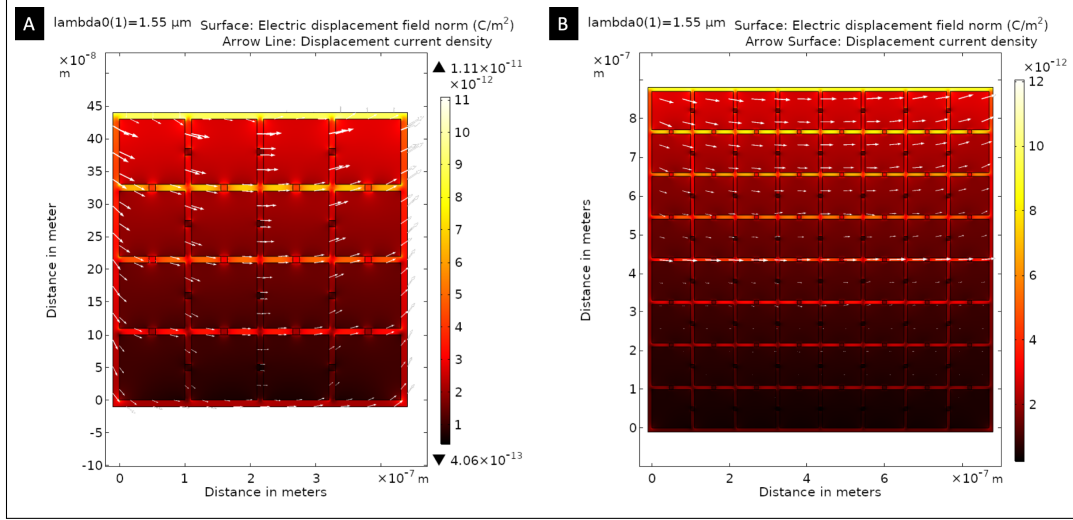


Figure 2.9: The epsilon-near-zero (ENZ) boxes in this simulation are $100 \text{ nm} \times 100 \text{ nm}$ and the epsilon very large (EVL) grooves are 10 nm wide where (A) contains 4 by 4 ENZ boxes and (B) contains 8 by 8. One can see that at longer length scales the electric displacement field continues to produce the form of the PDE solution, but the containment of displacement current density within the EVL air grooves is weakened.

displacement in the ENZ circuit board providing a perfect electric-circuit behavior.

However, a study of the size and scalability and their impact on the accuracy of the solution of the metatronic processor becomes absolutely determinant if the losses in the ENZ circuit board are not negligible as discussed in Section 2.6.4). Other parameters, such as width of the grooves and smoothness of the bending curves can impact the accuracy of the solution. The undesired influence of these parameters, here not discussed, would result in a systematic error that can be compensated or mitigated by accurate and controlled processes.

2.6.4 Monolithic Integration

In the past years, few materials have been considered for fabricating a metatronic circuit board, such as multilayered stacks of thin film [45, 46], NPs assemblies and graphene. However, their large-scale integration is far from easy.

We propose Indium tin oxide as suitable material for a monolithic integration of the proposed metatronic processor. ITO has a tunable and controllable ENZ position in the

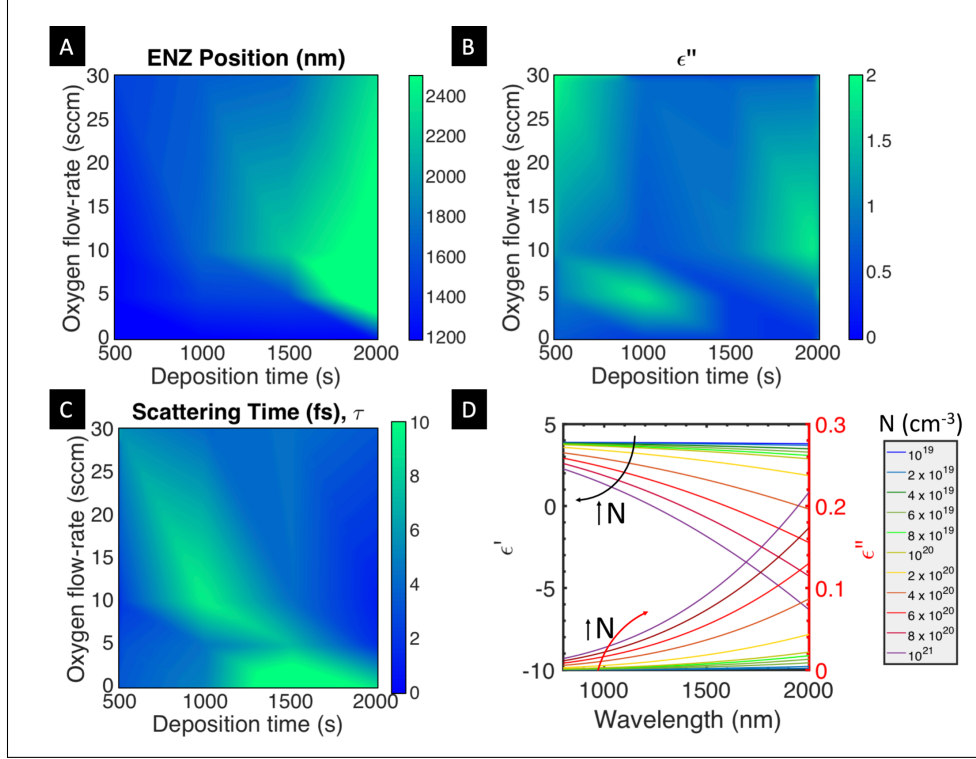


Figure 2.10: The (A) ENZ wavelength, (B) Electrostatic doping, and (C) Scattering Time (τ_{sc}) as function of process parameters (Oxygen flow-rate and deposition time). The (D) Drude model of ITO film, sputtered with an initial electron doping of 10^{19}cm^{-3} and $\Gamma = \frac{1}{\tau_{sc}}$, for an increasing carrier modulation (blue to red).

NIR, according to process parameters (e.g. Oxygen flow-rate, Thermal Annealing). Its optical properties, imaginary and real part of the permittivity, can be electrostatically tuned [47, 48], thus allowing GHz fast[49] energy efficient [50] reprogrammable features on the circuit board.

Moreover, recently, our group achieved a consistent control over ITO optical parameters in particular with respect to the ENZ wavelength as function of sputtering parameter, thus allowing to bridge the technological gap in the implementation of metatronic circuits [34]. According to our fundamental studies, depicted in figure 2.10, the ITO for the ENZ circuit board is supposed to be sputtered with 5 sccm Oxygen flow rate, enabling a 200 nm film in ENZ condition at 1550 nm, with not negligible losses $\tilde{\epsilon} = 0.3i$ which corresponds to a scattering time, $\Gamma = 2$ fs. The resistors, deposited using 20 sccm oxygen flow rate, which

yields to $\tilde{\varepsilon} = 1.2 + 0.8i$ and a scattering time of 5fs.

The major disadvantage is represented by the losses at ENZ condition. As a consequence of the losses in the ITO circuit board, the lines of the displacement field are not only contained in the air grooves, contrarily to the case of a ENZ material with negligible losses. In presence of non-negligible losses in the ENZ material, the circuit board is not completely insulating, since the displacement current is not negligible.

$$J_D = \frac{\partial D}{\partial t} = \varepsilon'' \omega E(\omega). \quad (2.11)$$

There are two major kinds of phenomena that impact the accuracy of the solution, both of which depend on the ITO losses. The first one, is a function of the mesh density and the second one of the total physical length of the circuit board. High density ($> 5 \times 5$) induces coupling within wires that shouldn't be connected, while the larger physical length ($> 2\mu\text{m}$) contributes to unwanted dissipation, deviating from the original solution.

Figure 2.11 plots the accuracy as function of the number of nodes and physical dimension of the circuit board. The maximum accuracy ($> 90\%$) is obtained for a $1\mu\text{m}$ grid, with a 4×4 mesh density. This is achieved thanks to the trade-off between mesh size and density, which minimizes the wire coupling, without extending the wiring length, producing unwanted losses.

The ITO is considered to be in a capacitor configuration, spaced by a thin dielectric, for electrostatic doping, enabling fine tuning of the permittivity values as well as updating of the problem.

The variation of the carrier density via gating in ITO affects both the resistance and the “reactance” in the metatronics equivalent circuit, hindering the accuracy of the solution, being Imaginary, and the real part of the permittivity in Kramer-Kronig relation. Nevertheless, contrarily to the resistive circuit, if either the boundary conditions or the impedances are quickly “refreshed”, the nano-optics equivalent circuit is substantially not affected by dispersion. In this case, the lumped circuit model still holds for high frequency modulation,

since even at 100s of GHz, the timescale at which the signal is modulated does so substantially slower than the time taken by the optical signal to travel through the nano-optics network.

2.6.5 ITO based Performance

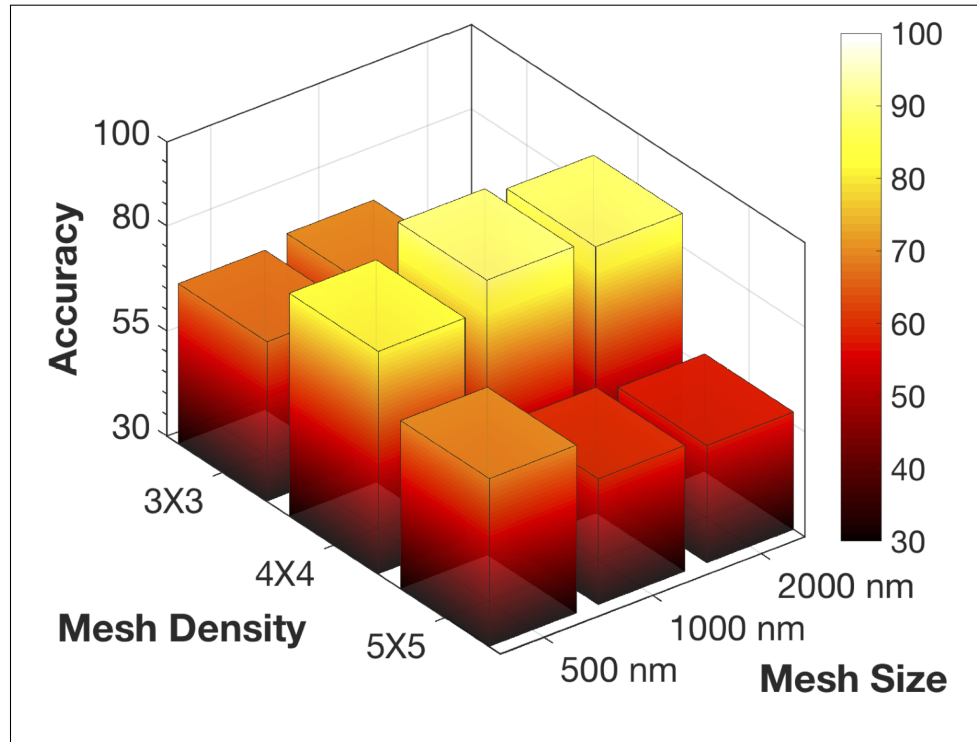


Figure 2.11: The metatronic solution accuracy as function of mesh density and size when compared to an discrete PDE solution.

The main limitation of the ITO metatronic processor are the unwanted losses in the circuit board. The losses affect both the power consumption and the accuracy of the solution. However, for a small size of the processor, an approximate solution is given. The accuracy is shown in terms of error computed with respect to the solution of a finite difference of comparable mesh density.

The power consumption from the processor is the summation of the optical power used for exciting the dipole (initiating the processor) and the the radio frequency power employed for modulating the carrier densities of each lumped elements, i.e. reprogramming

the circuit. Concerning the reconfigurability of the processor, recent works showed atto-joule efficient [50, 49] ITO based modulators operating at high speed. On the other hand, few mW optical power are needed for exciting the fluorescent molecule and setting the boundary conditions. Although, efficient measurements schemes must be used for detecting the electric field displacement at each node of the metatronic mesh, avoiding scanning over the sample, e.g. high resolution tip enhanced near field spectroscopy, in order to minimize the power used for the detection mechanism.

2.6.6 Near Field Displacement Measurement

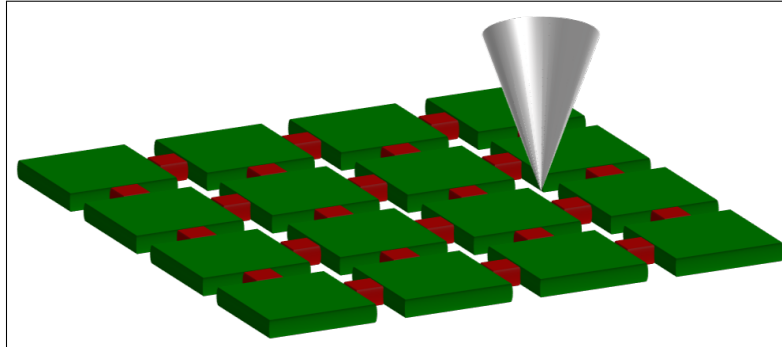


Figure 2.12: Schematic representation of a "Nanophotonic Probe". An impinging radiation excites a fluorescent molecule, creating a local near field, which produces an electric displacement in the metatronic circuit. The displacement is probed by the tips of a probe card, in a campanile tip aperture nSOM configuration.

In order to sample the electric field displacement signal at the nodes of the metatronic mesh, deep sub-wavelength near field microscopy has to be employed with nanometric spatial resolution [51, 52, 53]. Although, regular Near-field is associated with AFM systems, thus requiring long scanning time. In this section, we propose a Nano-optic probe card for reading of the values of the local displacement field as shown in Figure 2.12). The reading mechanism is based on multiple tips characterized by sub-wavelength aperture at the apex which collects the local near field radiation similarly to a local near field microscope, allowing for a parallel reading out. NSOM would be preferential with respect to Scattering type SNOM since the former will minimize the coupling between vertical dipoles, i.e.

metallic tip, introducing second order scattering and a higher degree of uncertainty in the system.

2.7 Supplemental Material

2.7.1 Analytical Solution to a Laplacian Steady State Heat Transfer PDE

Laplace's equation is a second-order partial differential equation which produces, as a solution, harmonic functions that accurately describe the behavior of electric, gravitational and fluid potentials. It has no time dependence, only a spatial dependence, and is often written as

$$\nabla^2 \varphi = 0 \quad (2.12)$$

where ∇^2 is the Laplace operator and φ is a scalar function.

For the purpose of simplicity, we will use Cartesian coordinate system and only discuss spatial variables x and y , which allows Laplace's equation to be rewritten as

$$\frac{\partial^2 \varphi}{\partial x^2} + \frac{\partial^2 \varphi}{\partial y^2} = 0 \quad (2.13)$$

which is equivalent to equation 2.12 for two dimensions. We are therefore solving a second order linear PDE. This describes a steady state system, and can be used for:

- steady state temperature distributions
- steady state stress distributions
- steady state potential distributions
- steady state flows

We will evaluate the problem over the rectangular region $0 \leq x \leq L, 0 \leq y \leq H$ for a fixed boundary temperature distribution.

$$\begin{aligned}
 \varphi(x, 0) &= f_1(x) \\
 \varphi(L, y) &= g_2(y) \\
 \varphi(x, H) &= f_2(x) \\
 \varphi(0, y) &= g_1(y)
 \end{aligned} \tag{2.14}$$

The four fixed boundary temperature distributes are non homogeneous, meaning that we cannot apply the separation of variables technique to solve the problem. However we can divide $\varphi(x, y)$ into its four components, where each component φ_i will satisfy one non-zero boundary condition and three zero boundary conditions.

$$\varphi(x, y) = \varphi_1(x, y) + \varphi_2(x, y) + \varphi_3(x, y) + \varphi_4(x, y) \tag{2.15}$$

With this in mind we will set our non-zero boundary condition to be at the top of our problem which will act as a heat source when we compare our analytical result to our electrical and optical solutions.

$$\begin{aligned}
 \text{BC1 : } \quad \varphi_3(x, 0) &= 0 \quad \text{for } 0 \leq x \leq L \\
 \text{BC2 : } \quad \varphi_3(L, y) &= 0 \quad \text{for } 0 \leq y \leq H \\
 \text{BC3 : } \quad \varphi_3(x, H) &= f_2(x) \quad \text{for } 0 \leq x \leq L \\
 \text{BC4 : } \quad \varphi_3(0, y) &= 0 \quad \text{for } 0 \leq y \leq H
 \end{aligned} \tag{2.16}$$

Now we can apply separation of variables to each φ_i function. For $\varphi_3(x, y)$ we set the

following

$$\varphi_3(x, y) = X(x)Y(y) \quad (2.17)$$

The three homogeneous boundary conditions will yield the following conditions

$$\begin{aligned} \text{BC1 : } X(x)Y(0) = 0 &\Rightarrow Y(0) = 0 \\ \text{BC2 : } X(L)Y(y) = 0 &\Rightarrow X(L) = 0 \\ \text{BC4 : } X(0)Y(y) = 0 &\Rightarrow X(0) = 0 \end{aligned} \quad (2.18)$$

Substitution of 2.17 into 2.13 yields

$$X''(x)Y(y) + X(x)Y''(y) = 0 \quad (2.19)$$

which is separated into

$$\frac{X''(x)}{X(x)} = -\frac{Y''(y)}{Y(y)} = k \quad (2.20)$$

where k is a constant equal to, greater than, or less than zero. The separation yields the following problems for X and Y

$$X(x)'' - kX(x) = 0, \quad X(0) = X(L) = 0 \quad (2.21)$$

and

$$Y(y)'' + kY(y) = 0, \quad Y(0) = 0 \quad (2.22)$$

For $X(x)$ we now need to find if a nontrivial solution exists for a value of k

1. Case $k > 0$

- (a) Boundary Value Problem: $X(x)'' - kX(x) = 0$, $X(0) = X(L) = 0$
- (b) General Solution: $X(x) = C_1e^{\sqrt{k}x} + C_2e^{-\sqrt{k}x}$
- (c) Boundary Condition: $X(0) = 0$ implies that $C_1 + C_2 = 0$, or $C_2 = -C_1$, so that $X(x) = C_1[e^{\sqrt{k}x} - e^{-\sqrt{k}x}] = 2C_1 \sinh(\sqrt{k}x)$
- (d) Boundary Condition: $X(L) = 0$ implies that $C_2 \sinh(\sqrt{k}L) = 0$, which is satisfied only if $C_2 = 0$. This follows from the fact that $\sinh(x)$ is zero only at $x = 0$.
- (e) Trivial Solution: The only solution to the boundary value problem for $k > 0$ is the trivial solution $X(x) = 0$.

2. Case $k = 0$

- (a) Boundary Value Problem: $X(x)'' = 0$, $X(0) = X(L) = 0$
- (b) General Solution: $X(x) = C_1x + C_2$
- (c) Boundary Condition: $X(0) = 0$ implies that $C_2 = 0$.
- (d) Boundary Condition: $X(L) = 0$ implies that $C_1L = 0$, or $C_1 = 0$.
- (e) Trivial Solution: The only solution to the case $k = 0$ is $X(x) = 0$

3. Case $k < 0$

- (a) Boundary Value Problems: $X(x)'' - kX(x) = 0$, $X(0) = X(L) = 0$
- (b) Define: $k = -\lambda$ so the $\lambda > 0$
- (c) General Solution: $X(x) = C_1 \cos(\sqrt{\lambda}x) + C_2 \sin(\sqrt{\lambda}x)$
- (d) Boundary Condition: $X(0) = 0$ implies that $C_1 + C_2 \cdot 0 = 0$ which implies that $C_1 = 0$
- (e) Boundary Condition: $X(L) = 0$ combined with $X(x) = C_2 \sin(\sqrt{\lambda}x)$ implies that $\sin(\sqrt{\lambda}L) = 0$

A nontrivial solution exists for $k < 0$. Since L is fixed, we must adjust λ in order that the above equation is satisfied. We set $k = -\lambda$, where $\lambda > 0$ gives

$$X(x)'' + \lambda X(x) = 0, \quad X(0) = 0, \quad X(L) = 0 \quad (2.23)$$

with eigenvalues of

$$\lambda = \lambda_n = \left(\frac{n\pi}{L}\right)^2, \quad n = 1, 2, 3, \dots \quad (2.24)$$

and associated eigenfunctions

$$X_n(x) = \sin\left(\frac{n\pi}{L}x\right) \quad (2.25)$$

Now consider the Y equation while recalling that $k = -\lambda$ so that $k_n = -\lambda_n$. The associated Y_n function will satisfy the differential equation

$$Y(y)'' - \left(\frac{n\pi}{L}\right)^2 Y(y) = 0, \quad Y(0) = 0 \quad (2.26)$$

Equation 2.26 is not longer a boundary value problem but is now an initial value problem with only one condition. The general solution can be written as

$$Y_n(y) = A_1 e^{n\pi y/L} + A_2 e^{-n\pi y/L} \quad (2.27)$$

but it is more convenient to use a hyperbolic functions

$$Y_n(y) = B_1 \cosh\left(\frac{n\pi y}{L}\right) + B_2 \sinh\left(\frac{-n\pi y}{L}\right) \quad (2.28)$$

The condition $Y(0) = 0$ implies that $B_1 = 0$. This is due to the fact that $\cosh(0) = 1$ and $\sinh(0) = 0$. Therefore for $Y_n(0)$ to equal 0, B_1 must equal 0. This shows that the

$Y_n(y)$ function associated with the $X_n(x)$ function is

$$Y_n(y) = B_2 \sinh\left(\frac{-n\pi y}{L}\right) \quad (2.29)$$

This results in the product solutions yielded by the separation of variables method up to a constant.

$$\varphi_{3,n}(x, y) = X_n(x) Y_n(y) = \sin\left(\frac{n\pi x}{L}\right) \sinh\left(\frac{n\pi y}{L}\right) \quad \text{for } n = 1, 2, 3, \dots \quad (2.30)$$

2.7.2 Mapping of Difference Equation Approximation to Electrical Resistance Mesh

$$\nabla \cdot \epsilon \nabla \varphi = g \quad (2.31)$$

The use of an electrical mesh allows us to generate the solution of an approximation of the partial differential equation 2.31 referred to from here on as the electrical difference equation solution. In the partial difference equation 2.31 where ϵ is the known scalar function, φ is the function, and $g = 0$ is the function relationship for a time independent Laplace second order partial differential equation. By performing linear interpolation on Figure 2.5 and disregarding the higher order terms we say that Equation 2.31 is asymptotically equal to:

$$\begin{aligned} \nabla \cdot \epsilon \nabla \varphi \simeq & \\ & \frac{2}{h_1 + h_3} \left[\frac{\epsilon_1}{h_1} (\varphi(\vec{P}_1) - \varphi(\vec{P}_0)) + \frac{\epsilon_3}{h_3} (\varphi(\vec{P}_3) - \varphi(\vec{P}_0)) \right] \\ & + \frac{2}{h_2 + h_4} \left[\frac{\epsilon_2}{h_2} (\varphi(\vec{P}_2) - \varphi(\vec{P}_0)) + \frac{\epsilon_4}{h_4} (\varphi(\vec{P}_4) - \varphi(\vec{P}_0)) \right] \end{aligned} \quad (2.32)$$

By setting neighboring points equal distant $h = h_1 = h_2 = h_3 = h_4$ and having a

constant scalar function $\epsilon = \epsilon_1 = \epsilon_2 = \epsilon_3 = \epsilon_4$

$$\begin{aligned} \nabla \cdot \epsilon \nabla \varphi \simeq & \\ & \frac{2}{h+h} \left[\frac{\epsilon}{h} (\varphi(\vec{P}_1) - \varphi(\vec{P}_0)) + \frac{\epsilon}{h} (\varphi(\vec{P}_3) - \varphi(\vec{P}_0)) \right] \\ & + \frac{2}{h+h} \left[\frac{\epsilon}{h} (\varphi(\vec{P}_2) - \varphi(\vec{P}_0)) + \frac{\epsilon}{h} (\varphi(\vec{P}_4) - \varphi(\vec{P}_0)) \right] \end{aligned} \quad (2.33)$$

By simplifying Eq. 2.33 you are left with

$$\nabla^2 \varphi \simeq \frac{1}{h^2} \left[\varphi(\vec{P}_1) + \varphi(\vec{P}_2) + \varphi(\vec{P}_3) + \varphi(\vec{P}_4) - 4(\varphi(\vec{P}_0)) \right] \quad (2.34)$$

Through the assignment of values and directions in Figure 2.5 and the application of Kirchoff's laws the following applies for $n = 1, n = 2, n = 3, n = 4$:

$$I_n = \frac{V_n - V_0}{R_n} \quad (2.35)$$

Kirchoff's laws also show that:

$$\sum_{n=1}^4 I_n = -I_0 \quad (2.36)$$

Eq. 2.35 and Eq. 2.36 result in:

$$\frac{V_1 - V_0}{R_1} + \frac{V_2 - V_0}{R_1} + \frac{V_3 - V_0}{R_3} + \frac{V_4 - V_0}{R_4} = -I_0 \quad (2.37)$$

By defining R_0 in the following manner

$$R_1 = R_2 = R_3 = R_4 = h^2 R_0 \quad (2.38)$$

and by defining the current I_0 fed into P_0 to be

$$I_0 = -g/R_0 \quad (2.39)$$

where g is the function relationship defined in Equation 2.31, a formal analogy can be shown between the voltages V_n appearing at the junctions and the sough function φ by comparing Equation 2.34 and a redefined Equation 2.37 through the definitions from Equation 2.38 and 2.39 in order show that

$$\nabla^2\varphi \simeq \frac{1}{h^2} [V_1 + V_2 + V_3 + V_4 - 4V_0] \quad (2.40)$$

The solution to the function φ in the differential equation Equation 2.31 has been approximated through the use of a difference equation. The solution is attained through measurement of voltage values at grid points. All that remains is to set the required boundary conditions to obtain the full solution if $g \equiv 0$ everywhere. If $g \neq 0$ currents from Equation 2.39 have to be fed into mesh points in order to use the resistive mesh to solve Poisson class PDEs. The resistance network performs the "relaxation technique" automatically and instantaneously for a Laplace equation.

Chapter 3 - Future Work

3.1 Future Work

3.1.1 Year 3 from October 2019 to September 2020

Going forward I would like to work on the metatronic fabrication effort since I have spent most of my research time thus far working on understanding the mathematical underpinning of finite difference computing, writing software, and building computational models. One of the initial challenges metatronically will be constructing nanophotonic local near field probes that readout all displacement current mesh points in parallel.

3.1.2 Year 4 from October 2020 to September 2021

In the final year I hope I will be able to program a fabricated metatronic ROC to be used as an analog accelerator within a numerical parallel multi grid method to see if we can demonstrate computational time complexity speedups over purely software based implementations.

3.2 Concluding Thoughts

The concept of an analog mesh based PDE solving co-processor is interesting to anyone who wants to improve the computational time complexity of their algorithm regardless of the physical phenomena utilized to perform by maintaining analog operations in constant time $O(1)$ as shown in Figure 2.1.

In order to make up for an analog computers lack a flexibility compared to a digital transistor CMOS based architecture, the analog alternative must also provide flexibility of problem types within its problem domain. This is accomplished through the use of resistors, capacitors, and inductors electrically, and the real and imaginary components of relative permittivity at material interfaces metatronically as shown in Figure 1.3.

In the investigation of the photonic and metatronic implementations of ROC, we note that the metatronic architecture exhibits increasing accuracy with increasing node density as shown in Figure 1.5, in the same fashion as the electric node density as shown in Figure 1.4. However the metatronic circuit has an optical refresh rate in the Terahertz as opposed to the electrical Gigahertz refresh rate. This means that the upper limit to the write time, or clock speed, for the Metatronic circuit is higher than that of the electric circuit because the metatronic circuit will remain in the lumped element domain for higher frequencies than the electric circuit while still abiding by Shannon-Hartley theorem limit.

The large size of the photonic mesh and its relatively short optical operation wavelength results in a distributed circuit, changing the physics of optical node splitting from neighborhood defined to geometrically defined, as shown the Figure 1.2, and thus causing decreased accuracy with increased photonic node density as noted in Figure 1.5.

The Metatronic solution operates at the same short operation wavelength as the Photonic circuit, but due to the metatronic circuits nanoscale dimension it operates as a lumped element and thus retains its increasing density increasing accuracy behavior, while still allowing for pde reconfiguration utilizing metatronic capacitance and inductance due to the change in sign of real component of the relative permittivity at material interfaces. Metatronics retains, the computational complexity shown in Figure 1.5, accuracy density behavior shown in Figure 1.5, and reconfigurability advantages of electronics while allowing for an increased upper limit write time, or clock speed. This novelty merits the fabrication of metatronic ROC.

References

- [1] Y. Li, I. Liberal, C. Della Giovampaola, and N. Engheta, “Waveguide metatronics: Lumped circuitry based on structural dispersion,” *Science advances*, vol. 2, no. 6, e1501790, 2016.
- [2] M. Snir, *Parallel computing 2020: Preparing for the post-moore era*.
- [3] “International technology roadmap for semiconductors 2.0 2015 edition executive report,” ITRS, Tech. Rep., 2015.
- [4] “International roadmap for devices and systems 2017 edition,” IEEE, Tech. Rep., 2017.
- [5] K. Vissers, “Versal: The xilinx adaptive compute acceleration platform (acap),” in *Proceedings of the 2019 ACM/SIGDA International Symposium on Field-Programmable Gate Arrays*, ACM, 2019, pp. 83–83.
- [6] G Liebmann, “Solution of partial differential equations with a resistance network analogue,” *British Journal of Applied Physics*, vol. 1, no. 4, p. 92, 1950.
- [7] ———, “Resistance-network analogues with unequal meshes or subdivided meshes,” *British Journal of Applied Physics*, vol. 5, no. 10, p. 362, 1954.
- [8] J. Ramirez-Angulo and M. R. DeYong, *Digitally-configurable analog vlsi chip and method for real-time solution of partial differential equations*, US Patent 6,141,676, 2000.
- [9] V. J. Sorger, S. Sun, T. El-ghazawi, A. h. A. Badawy, and V. K. Narayana, “Reconfigurable optical computer,” pat. 20 170 161 417, 2017.
- [10] I. H. Herron and M. R. Foster, *Partial Differential Equations in Fluid Dynamics*. Cambridge University Press, 2008, ISBN: 0521888247.
- [11] M. N. O. Sadiku and L. C. Agba, “A simple introduction to the transmission-line modeling,” *IEEE Transactions on Circuits and Systems*, vol. 37, no. 8, pp. 991–999, 1990.
- [12] H. Berestycki and Y. Pomeau, *Nonlinear PDE’s in Condensed Matter and Reactive Flows*. Dec. 2002, ISBN: 9789401003070.
- [13] A. Selvadurai, *Partial Differential Equations in Mechanics I: Fundamentals, Laplace’s Equation, Diffusion Equation, Wave Equation*. Apr. 2000, ISBN: 9783662040065.

- [14] H. Y.J.Y.S. L. C. Tang Q. Mi, “Pde (ode)-based image processing methods for optical interferometry fringe,” 2013.
- [15] E. Rocca and R. Rossi, ““entropic” solutions to a thermodynamically consistent pde system for phase transitions and damage,” *SIAM Journal on Mathematical Analysis*, vol. 47, no. 4, pp. 2519–2586, 2015.
- [16] I. Richter, K. Pas, X. Guo, R. Patel, J. Liu, E. Ipek, and E. G. Friedman, “Memristive accelerator for extreme scale linear solvers,” in *Government Microcircuit Applications & Critical Technology Conference (GOMACTech)*, 2015.
- [17] J. Zhu, *Solving Partial Differential Equations on Parallel Computers an Introduction*. World Scientific Pub Co Inc, 1994, ISBN: 9810215789.
- [18] L. Pinuel, I. Martin, and F. Tirado, “A special-purpose parallel computer for solving partial differential equations,” pp. 509–517, 1998.
- [19] J.Dongarra, “Current trends in high performance computing and challenges for the future,” *AMC Learning Webinar held on February 7, 2017*.
- [20] P. Palmer, A. R. Copson, and S. Redshaw, “Investigations into the use of an electrical resistance analogue for the solution of certain oscillatory-flow problems,” *Aero. Res. Counc. R & M*, no. 3121, 1959.
- [21] J. Ramirez-Angulo and M. R. DeYong, *Digitally-configurable analog vlsi chip and method for real-time solution of partial differential equations*, US Patent 6,141,676, 2000.
- [22] A. Hastings, *The Art of Analog Layout (2nd Edition)*. Pearson, 2005, ISBN: 0131464108.
- [23] “Electronics resurgence initiative: Page 3 investments architectures thrust,” Defense Advanced Research Project Agency, Tech. Rep., 2017.
- [24] R. M.X. Z. V.J. Sorger N.D. Lanzillotti-Kimura, “Ultra-compact silicon nanophotonic modulator with broadbandresponse,” *Nanophotonics*, vol. 1, no. 1, 2012.
- [25] A. Mehrabian, Y. Al-Kabani, V. J. Sorger, and T. A. El-Ghazawi, “PCNNA: A photonic convolutional neural network accelerator,” *CoRR*, vol. abs/1807.08792, 2018. arXiv: 1807.08792.
- [26] S. Sun, V. K. Narayana, I. Sarpkaya, J. Crandall, R. A. Soref, H. Dalir, T. El-Ghazawi, and V. J. Sorger, “Hybrid photonic-plasmonic nonblocking broadband 5 5 router for optical networks,” *IEEE Photonics Journal*, vol. 10, no. 2, pp. 1–12, 2018.

- [27] N. Mohammadi Estakhri, B. Edwards, and N. Engheta, “Inverse-designed metas-structures that solve equations,” *Science*, vol. 363, no. 6433, pp. 1333–1338, 2019. eprint: <http://science.sciencemag.org/content/363/6433/1333.full.pdf>.
- [28] G. Tsoulos, *MIMO system technology for wireless communications*. CRC press, 2006.
- [29] M. Hu, J. P. Strachan, Z. Li, E. M. Grafals, N. Davila, C. Graves, S. Lam, N. Ge, J. J. Yang, and R. S. Williams, “Dot-product engine for neuromorphic computing: Programming 1t1m crossbar to accelerate matrix-vector multiplication,” in *Proceedings of the 53rd annual design automation conference*, ACM, 2016, p. 19.
- [30] M. N. Bojnordi and E. Ipek, “Memristive boltzmann machine: A hardware accelerator for combinatorial optimization and deep learning,” in *2016 IEEE International Symposium on High Performance Computer Architecture (HPCA)*, IEEE, 2016, pp. 1–13.
- [31] H. N.V. S. J. George, “Towards on-chip optical ffts for convolutional neural networks,” *IEEE International Conference on Rebooting Computing (ICRC)*, 2017.
- [32] M. Alioto, “Energy-quality scalable adaptive vlsi circuits and systems beyond approximate computing,” *Design, Automation —& Test in Europe Conference —& Exhibition*, 2017.
- [33] N. Engheta, “Circuits with light at nanoscales: Optical nanocircuits inspired by meta-materials,” *Science*, vol. 317, no. 5845, pp. 1698–1702, 2007.
- [34] Y. Gui, M. Miscuglio, Z. Ma, M. T. Tahersima, H. Dalir, and V. J. Sorger, “Impact of the process parameters to the optical and electrical properties of rf sputtered indium thin oxide films: A holistic approach,” *arXiv preprint arXiv:1811.08344*, 2018.
- [35] R. Amin, R. Maiti, C. Carfano, Z. Ma, M. H. Tahersima, Y. Lilach, D. Ratnayake, H. Dalir, and V. J. Sorger, “0.52 v mm ito-based mach-zehnder modulator in silicon photonics,” *APL Photonics*, vol. 3, no. 12, p. 126 104, 2018.
- [36] Z. Ma, Z. Li, K. Liu, C. Ye, and V. J. Sorger, “Indium-tin-oxide for high-performance electro-optic modulation,” *Nanophotonics*, vol. 4, no. 1, pp. 198–213, 2015.
- [37] A. Alu, V. Shalaev, M. Loncar, and V. J. Sorger, “Metasurfaces - from science to applications,” *Nanophotonics*, vol. 7, no. 6, pp. 949–951, 2018.
- [38] M. H. Tahersima, M. D. Birowosuto, Z. Ma, W. C. Coley, M. D. Valentin, S. Naghibi Alvillar, I.-H. Lu, Y. Zhou, I. Sarpkaya, A. Martinez, *et al.*, “Testbeds for transition metal dichalcogenide photonics: Efficacy of light emission enhancement in

monomer vs dimer nanoscale antennae,” *ACS Photonics*, vol. 4, no. 7, pp. 1713–1721, 2017.

- [39] E. R. Vrscaj, *Amath 353: Partial differential equations i*, 2010.
- [40] N. M. Estakhri, B. Edwards, and N. Engheta, “Inverse-designed metastructures that solve equations,” *Science*, vol. 363, no. 6433, pp. 1333–1338, 2019.
- [41] A. Vakil and N. Engheta, “Transformation optics using graphene,” *Science*, vol. 332, no. 6035, pp. 1291–1294, 2011.
- [42] A. Alu, M. G. Silveirinha, A. Salandrino, and N. Engheta, “Epsilon-near-zero metamaterials and electromagnetic sources: Tailoring the radiation phase pattern,” *Physical review B*, vol. 75, no. 15, p. 155 410, 2007.
- [43] P. Moitra, B. A. Slovick, Z. Gang Yu, S. Krishnamurthy, and J. Valentine, “Experimental demonstration of a broadband all-dielectric metamaterial perfect reflector,” *Applied Physics Letters*, vol. 104, no. 17, p. 171 102, Apr. 2014.
- [44] Y. Li, S. Kita, P. Muñoz, O. Reshef, D. I. Vulis, M. Yin, M. LonÄar, and E. Mazur, “On-chip zero-index metamaterials,” *Nature Photonics*, vol. 9, no. 11, pp. 738–742, Nov. 2015.
- [45] Y. Li, I. Liberal, C. Della Giovampaola, and N. Engheta, “Waveguide metatronics: Lumped circuitry based on structural dispersion,” *Science Advances*, vol. 2, no. 6, 2016. eprint: <http://advances.sciencemag.org/content/2/6/e1501790.full.pdf>.
- [46] Y. Li and N. Engheta, “Capacitor-inspired metamaterial inductors,” *Phys. Rev. Applied*, vol. 10, p. 054 021, 5 2018.
- [47] V. J. Sorger, N. D. Lanzillotti-Kimura, R.-M. Ma, and X. Zhang, “Ultra-compact silicon nanophotonic modulator with broadband response,” *Nanophotonics*, vol. 1, no. 1, pp. 17–22, 2012.
- [48] R. Amin, R. Maiti, C. Carfano, Z. Ma, M. H. Tahersima, Y. Lilach, D. Ratnayake, H. Dalir, and V. J. Sorger, “0.52 V mm ITO-based Mach-Zehnder modulator in silicon photonics,” *APL Photonics*, vol. 3, no. 12, p. 126 104, Dec. 2018.
- [49] H. Dalir, F. Mokhtari-Koushyar, I. Zand, E. Heidari, X. Xu, Z. Pan, S. Sun, R. Amin, V. J. Sorger, and R. T. Chen, “Atto-Joule, high-speed, low-loss plasmonic modulator based on adiabatic coupled waveguides,” *Nanophotonics*, vol. 7, no. 5, pp. 859–864, 2018.

- [50] R. Amin, J. George, J. Khurgin, T. El-Ghazawi, P. R. Prucnal, and V. J. Sorger, “Attojoule Modulators for Photonic Neuromorphic Computing,” in *Conference on Lasers and Electro-Optics (2018)*, paper *ATH1Q.4*, Optical Society of America, May 2018, ATH1Q.4.
- [51] W. Bao, M. Melli, N. Caselli, F. Riboli, D. S. Wiersma, M. Staffaroni, H. Choo, D. F. Ogletree, S. Aloni, J. Bokor, S. Cabrini, F. Intonti, M. B. Salmeron, E. Yablonovitch, P. J. Schuck, and A. Weber-Bargioni, “Mapping Local Charge Recombination Heterogeneity by Multidimensional Nanospectroscopic Imaging,” *Science*, vol. 338, no. 6112, pp. 1317–1321, Dec. 2012.
- [52] W. Bao, N. J. Borys, C. Ko, J. Suh, W. Fan, A. Thron, Y. Zhang, A. Buyanin, J. Zhang, S. Cabrini, P. D. Ashby, A. Weber-Bargioni, S. Tongay, S. Aloni, D. F. Ogletree, J. Wu, M. B. Salmeron, and P. J. Schuck, “Visualizing nanoscale excitonic relaxation properties of disordered edges and grain boundaries in monolayer molybdenum disulfide,” *Nature Communications*, vol. 6, p. 7993, Aug. 2015.
- [53] N. Caselli, F. La China, W. Bao, F. Riboli, A. Gerardino, L. Li, E. H. Linfield, F. Pagliano, A. Fiore, P. J. Schuck, S. Cabrini, A. Weber-Bargioni, M. Gurioli, and F. Intonti, “Deep-subwavelength imaging of both electric and magnetic localized optical fields by plasmonic campanile nanoantenna,” *Scientific Reports*, vol. 5, p. 9606, Jun. 2015.

Appendices

Appendix A - Software Development

A.1 GitHub

The software repository used to call simulations via their API's and plot output data is located in the private repository roc grid simulation

https://github.com/openhpclgw/roc_grid_simulation located within the GitHub Organization OPEN HPCL Collaboration at

<https://github.com/openhpclgw>. Engin Kayraklioglu developed the master branch of the Github repository, which I branched into my own work space named boundaryConditions, in which I wrote all my data processing Python code.

Appendix B - Computational Models

B.1 Computation

B.1.1 Computing Resources

The computations performed in this thesis utilize a variety of software tools described in Section B.2 and well as developed source code described in Section A.1 where all computation has access to the same resources which are as follows: MacBook Pro (15-inch, Late 2016), Processor 2.9 GHz Intel Core i7, Memory 16 GB 2133 MHz LPDDR3, Graphics Radeon Pro 460 4 GB Intel HD Graphics 530 1536 MB.

B.2 Simulation Tools and Applications

B.2.1 COMPSOL Multiphysics

I used COMSOL Multiphysics to solve a heat transfer partial differential equation numerically in order to have a comparison for Photonic ROC and Metatronic ROC analog solutions. I also used COMSOL Multiphysics to simulate Metatronic ROC at different mesh scales.

B.2.2 Lumerical Interconnect

I used Lumerical Interconnect to view and understand the schematic of the Photonic ROC.

B.2.3 Wolfram Mathematica

I used Wolfram Mathematica to visualize the discretization of an analytical PDE solution.

B.2.4 Simulation Program with Integrated Circuit Emphasis (SPICE)

I use SPICE within my bounadryConditions Python code to generate and simulate an analog electrical resistance grid at different mesh scales.